Spring 2024

RESPIRATORY-MOTION MATCHED ATTENUATION CORRECTION FOR DUAL-GATED CARDIAC SINGLE PHOTON EMISSION COMPUTED TOMOGRAPHY (SPECT)

Christina Xing
The University of Texas at Arlington

RESPIRATORY-MOTION MATCHED ATTENUATION CORRECTION FOR DUAL-GATED CARDIAC SINGLE PHOTON EMISSION COMPUTED TOMOGRAPHY (SPECT)

By

Christina Xing

THESIS

Submitted in partial fulfillment of the requirements for the degree of
Master of Science in Physics at
The University of Texas at Arlington
May 2024

Arlington, Texas

Supervising Committee:

Dr. Mingwu Jin, Supervising Professor
Dr. Qiming Zhang
Dr. Yujie Chi

ACKNOWLEDGMENTS

I would like to express my gratitude and appreciation to my supervising professor, Dr. Mingwu Jin, for his invaluable advice, guidance, and support throughout my academic journey. Additionally, I extend my sincere thanks to my lab colleague, Dr. Shiwei Zhou, whose expertise in programming has been instrumental in shaping the trajectory of my research endeavors.

Furthermore, I wish to extend my heartfelt gratitude to Dr. Yujie Chi and Dr. Qiming Zhang for dedicating their time and expertise to serve on my committee, thereby enriching my academic pursuits.

I express my gratitude to all my professors and professional staff of the Department of Physics for their support throughout my academic journey. I am particularly grateful to Ms. Stacey Cody and Mr. Victor Reece for their direct and indirect assistance over the years. I extend my profound gratitude to the Chair of the Physics department, Dr. Alex Weiss, my undergraduate research advisor, Dr. Ramon Lopez, and my professors Dr. Haleh K Hadavand, Dr. Ben Jones, Dr. Raquel Castillo Fernandez, Dr. Ali Koymen, Dr. Frederick Wilder, and Dr. Jonathan Asaadi for their continuous encouragement, guidance, and support. Additionally, I would like to thank Dr. Suman Satyal and Dr. Madhab Pokhrel for their roles as supporting lab coordinators.

This work is supported in part by in part by NIH under Grant No. 1R15HL150708-01A1.

ABSTRACT OF THE THESIS

RESPIRATORY-MOTION MATCHED ATTENUATION CORRECTION FOR DUAL-GATED CARDIAC SINGLE PHOTON EMISSION COMPUTED TOMOGRAPHY (SPECT)

by

Christina Xing

Master of Science in Physics

The University of Texas at Arlington, 2024

Dr. Mingwu Jin, Supervising Professor

Cardiac and respiratory dual-gated single-photon emission computed tomography (SPECT) is a promising technique for minimizing the motion artifacts in myocardial perfusion imaging (MPI). However, attenuation correction (AC) for dual-gated SPECT using an attenuation map averaged over the respiratory cycle may lead to mismatched attenuation correction artifacts. In this study, we propose a respiratory motion-matched attenuation correction (RMM-AC) to further improve dual-gated SPECT. For each respiratory gate, RMM-AC uses an attenuation map that matches the SPECT image in a 4D reconstruction framework. Filtered backprojection reconstruction without AC (FBP-nAC) and 4D reconstruction with the attenuation map averaged over all respiratory gates (AVE-AC) are used for comparison. We used the NCAT phantom and SIMIND Monte Carlo simulation to simulate dual-gated cardiac SPECT using ^{99m}Tc-sestamibi. An ischemic lesion with 20% uptake reduction at four locations of the left ventricular myocardium was used for a channelized Hotelling observer (CHO) study. Three methods were quantitatively

evaluated using the root mean squared error (RMSE) and the area under the receiver operating characteristic (ROC) curve (Az) of CHO. RMM-AC outperforms FBP-nAC and AVE-AC in both metrics, which reflects improvements on both reconstruction accuracy and lesion detectability. This study paves a way for its adaption of the clinical dual-gated cardiac SPECT MPI.

TABLE OF CONTENTS

LIST OF FIGURES

Illustration Page

LIST OF TABLES

Table Page

LIST OF ABBREVIATIONS

18F-FDG	18F-fluorodeoxyglucose
^{201}Tl	Thallium-201
^{99m}Tc	Technetium-99m
AC	Attenuation correction
AVE-AC	Attenuation map averaged over all respiratory gates
CAD	Coronary artery disease
CBCT	Cone-beam CT
CHO	Channelized Hotelling observer
CT	Computed tomography
C-SPECT	Cardiac-gated SPECT
DAP	Defect absent phantom
DPP	Defect present phantom
D-SPECT	Dual cardiac-respiratory gated SPECT
ECG	Electrocardiogram
ET	Emission tomography
FDG	F-fluorodeoxyglucose
MCAT	Mathematical Cardiac-Torso Phantom
MPI	Myocardial perfusion imaging
NCAT	NURBS-based Cardiac-Torso Phantom
NURBS	Non-Uniform Rational B-Splines
pdfs	Probability density functions
PET	Positron Emission Tomography

PMT	Photomultiplier tubes
ROC	Receiver operating characteristic
RMM-AC	Respiratory motion-matched attenuation correction
RMSE	Root mean squared error
SPECT	Single Photon Emission Computed Tomography

Chapter 1

Introduction

1.1. Emission Tomography (ET)

Single Photon Emission Computed Tomography (SPECT) uses radioactive materials to image the physiological properties of the living body [1]. It is one of the techniques that stem from emission tomography (ET). Emission tomography is different from x-ray computed tomography (CT). Rather than offering anatomical details, it plays an essential role in detecting abnormalities through the radiotracer distribution targeting functional properties, such as glucose metabolism and blood flow, and thus acts as a functional imaging approach [2]. Emission tomography combines two fundamental principles: gamma-ray emission imaging, known as the tracer principle, and volumetric imaging of the body's interior, known as tomography [2]. The tracer principle is a pivotal concept in nuclear medicine, molecular imaging, and radiotheranostics [3,4]. The tracer principle was developed in the early 1900s by the Nobel Prize winner, George de Hevesy. The discovery of the tracer principle came after an initial setback in 1911, when de Hevesy's attempted to separate radioactive lead from stable lead was unsuccessful from request made by Ernest Rutherford [3,4,5]. Through the experiment, the tracer principle states that radioactive compounds interact with an organism's physiological processes similar to nonradioactive materials. Due to radioactive materials can be detected by its emission of gamma rays, it was further validated that the tiny amount of radioisotops can be used to track the vital substance flow and distribution within the body [2]. Another significant advantage of the tracer principle as a foundation for imaging biological processes in humans were due to the ability to detect even minuscule amounts of radioactive material, the tracer principle enables the measurement of molecular concentrations with exceptional sensitivity. In addition, tracer

measurements are noninvasive, as the concentration of the tracer is deduced from gamma ray counts (high-energy photons) emitted from within the body as a result of the administered tracer's radioactive decay[2].

To better understand how a radiopharmaceutical ("radiotracer" or "tracer") works, ^{18}F-fluorodeoxyglucose (^{18}F-FDG) can be used as an example. ^{18}F-FDG serves as a tracer for assessing glucose metabolism and comprises two constituents: (1) FDG, an analogue of glucose, and (2) a fluorine-18 label (^{18}F), enabling the detection of the tracer through counting of annihlation gamma-ray photons (511keV) from the emitted positrons of F-18. Upon entry into cells, ^{18}F-FDG follows the same uptake pathway as glucose but undergoes metabolism within the cell to form a new compound, a metabolite, which remains trapped within the cell. Consequently, the concentration of the radioactive metabolite increases over time in proportion to the cell's glucose metabolic rate. By injecting of ^{18}F-FDG into the body, it will enable to quantifying local levels of glucose metabolism [2]. Gamma rays can pass through body and appear to be translucent, while the radiotracer would appear to be glowing translucent substance [2].

Tomography is another important principle behind emission tomography. A tomography image refers to a picture of a cross-sectional slice of the body and it is calculated by computer from the projection measurements, also refers to image reconstruction [2]. To delve into the comprehension of projection and tomographic images and their interrelation, we will focus on the section of the body lying within a specific slice plane with two frames of reference. The first one is the fixed patient's frame of reference, characterized by coordinates (x, y). The second one is the rotating frame, described by coordinates (x_r, y_r) with a rotation angle ϕ. This rotating frame can be treat as a hypothetical observer, who can move around the patient to observe the body's interior from different angles. Additionally, let's define f(x, y) as the distribution of radiotracer within the

body slice defined by the xy plane [2].

The parallel projection is defined as the line integral of (x, y) along the y_r axis when viewed at angle ϕ, denoted as $p(x_r, \phi) = \int f(x, y)dy_r$ as shown in Fig. 1. In simpler terms, at a given angle ϕ, the projection represents the integration of the radiotracer distribution along lines of sight parallel to the y_r axis [2]. Measurement of these projections are obtained from various perspectives around the body (i.e., for multiple values of ϕ). The goal of tomography is to deduce the radiotracer distribution f(x, y) from these projection data. In modern ET imaging systems, projections are acquired for multiple slice planes simultaneously (i.e., for various values of the z coordinate). This allows reconstruction of a three-dimensional (3D) radiotracer distribution f(x, y, z). Moreover, most imaging systems collect projection data for lines of sight not confined to parallel 2D planes. To effectively utilize this broader range of data, fully 3D image-reconstruction techniques have been developed, treating the body as a unified 3D object rather than a stack of 2D slices.

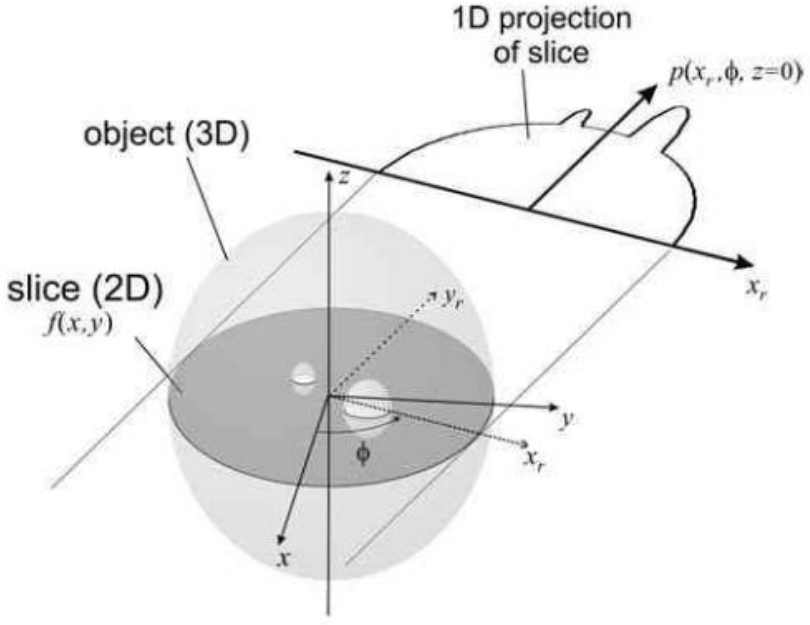

Figure 1 One-dimensional parallel projection of a two-dimensional slice through an object [2].

There are four key steps in an emission tomography study: 1) radiopharmaceutical production; 2) the administration of radiopharmaceutical which can be either by injection or by inhalation; 3) data acquisition, in which information regarding the position and direction of each gamma ray is measured, and the results are compiled into a histogram of discrete position-direction bins. These histogram bins contain measurements of the projections; and 4) image reconstruction, where the acquired projection data from the imaging system is utilized to generate the desired tomographic images. A common method for image reconstruction in clinic is an analytical technique known as filtered backprojection (FBP). An additional step of image analysis could be included [2].

1.2 Single Photon Emission Computed Tomography (SPECT)

The main emission tomography techniques are Single Photon Emission Computed Tomography (SPECT) and Positron Emission Tomography (PET) due to the suitable chemical and physical properties of radioisotopes used in the tracer [2]. Radioactive decay is the process wherein the nucleus of an unstable atom releases energy through the spontaneous emission of ionizing radiation, including photons, alpha particles, and beta particles. This process can occur internally within the nucleus of the unstable atom and occasionally involve an inner electron of the radioactive atom, such as electron capture and internal conversion. Unstable atoms demonstrating this property of radioactive decay are referred to as radionuclides or radioisotopes, which can occur naturally or be artificially produced [7].

One of the most commonly used radioisotopes in SPECT is technetium-99m (Tc-99m or ^{99m}Tc). It undergoes decay with a half-life of 6.006 hours and a primary photon energy of 140 keV (89%), ultimately decaying to technetium-99. ^{99m}Tc is typically produced from a generator using

the longer-lived molybdenum-99 (with a half-life of 2.75 days), as shown in Figure 2, allowing for the availability of the isotope for medical use on-site [7].

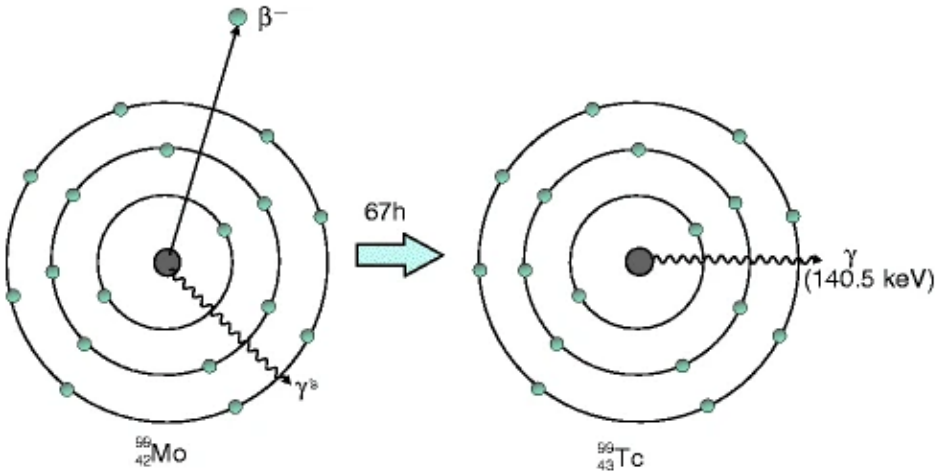

Figure 2. Schematic diagram of the production of ^{99m}Tc from the parent ^{99}Mo [7]

The energy emitted by ^{99m}Tc falls within the optimal range for efficient detection using current scintillation gamma camera technology. Coupled with its convenient half-life—long enough to facilitate radiolabeling and imaging procedures yet short enough to minimize unnecessary radiation exposure to patients—^{99m}Tc stands out as an appealing option for nuclear medical imaging. Moreover, its on-site production from the longer-lived parent radionuclide further enhances its popularity in nuclear planar imaging and SPECT [7].

Single-photon detection relies on sophisticated physical collimation to precisely capture directional data from incoming photons. In order to generate an image of the distribution of radiopharmaceuticals, establishing a correspondence between points in the object and points in the image is important. Unlike conventional photographic cameras, which utilize lenses to refract light rays and form images on film or detector arrays, gamma rays are too energetic to be captured using standard lenses. An essential component known as a collimator constructed from a thick sheet of dense material like lead, the collimator resembles a honeycomb, perforated with long, slender channels. The collimator functions by selectively allowing only those rays traveling in or close to

a specific direction, aligned with the orientation of its channels, different from than lens that redirects rays. Collimator hole dimensions typically range from 1.4 to 3.0 mm in diameter, with a bore length spanning between 24 and 60 mm, ensuring optimal performance in photon capture and directionality [7]. Gamma rays traveling in other directions are either obstructed by the channel walls or bypass the collimator [2].

The collimator displayed in Figure 3 is an example of a parallel-hole design, where all channels are aligned in parallel. When the face of the collimator is oriented in a specific direction, denoted as 'ϕ' the resulting image comprises the previously defined projections. Although the projections formed by a collimator may not precisely represent line integrals of the object distribution due to various factors, the fundamental concept of SPECT imaging can be grasped by understanding these simple projections shown in Figure 3 [2].

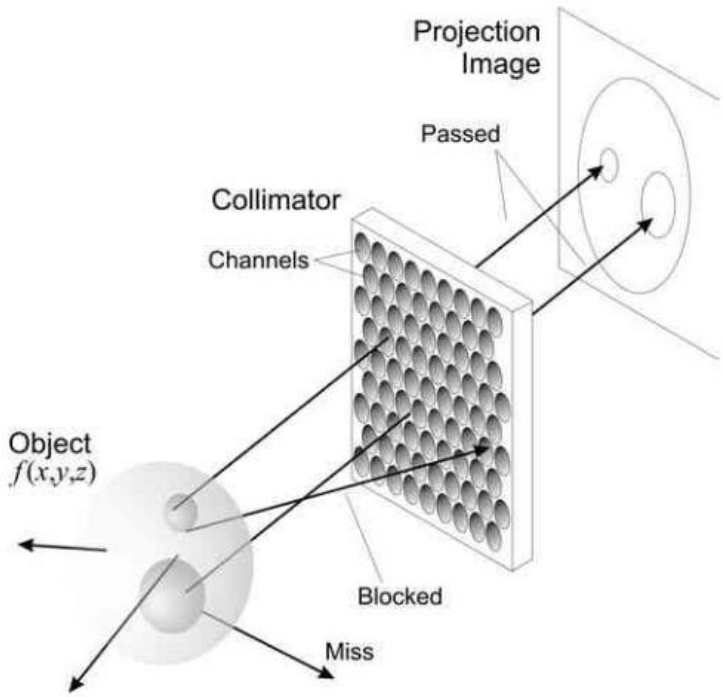

Figure 3. A collimator forms an image of the object by passing only rays traveling in a particular direction [2]

The heart of a SPECT system is the scintillation gamma camera, also known as the Anger

camera [2]. When a gamma ray successfully passes through the collimator, it strikes the initial component of the detection apparatus, a scintillator crystal (usually sodium iodide (NaI)). This crystal utilizes the energy from the high-energy gamma-ray to generate numerous photons at optical wavelengths. These photons are then detected by an array of photomultiplier tubes (PMTs), which are operating on the principle of the photoelectric effect[2]. From a single photoelectron, a PMT can generate a cascade of electrons, resulting in a measurable electrical current. This current is detected by accompanying electronics, which record the occurrence of an event. Relative readings from PMTs situated near the gamma ray's point of impact are utilized to calculate the two-dimensional spatial coordinates of the gamma-ray event relative to the camera's face. These events are then aggregated into a histogram based on their respective positions[2]. After numerous events have been tallied, the resulting histogram forms a projection image of the object. However, the measured projection image often exhibits noticeable noise, resulting from random fluctuations that compromise image fidelity [2].

To obtain the projection images necessary for image reconstruction, the patient is imaged repeatedly from various perspectives by rotating the gamma camera around the patient. Modern SPECT systems expedite this process and enhance gamma-ray capture by utilizing two or three cameras simultaneously positioned around the patient to capture multiple projection images concurrently [2].

Figure 4 demonstrates a diagram of a conventional gamma camera used in SPECT [2]. As can be seen, the collimator constructs an image of the patient on the scintillation crystal, where gamma rays are transformed into light. This light is captured by PMTs, and their outputs are digitized for calculating the spatial coordinates of each gamma-ray event concerning the camera's surface. Subsequently, a computer is utilized for processing, storing, and displaying the images[2].

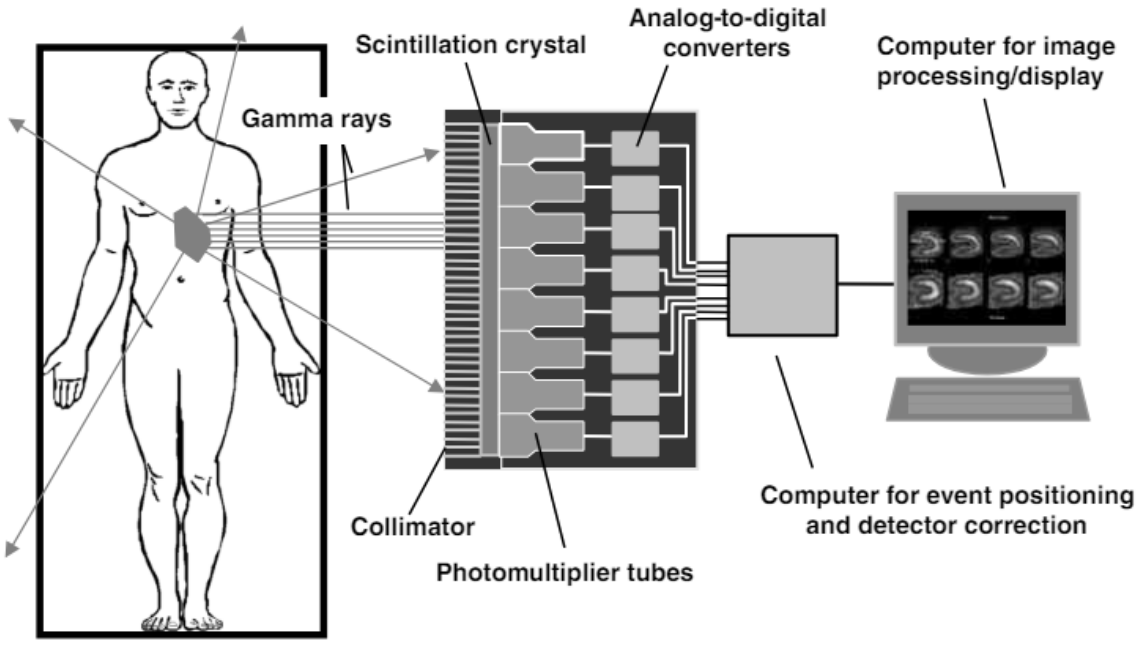

Figure 4. Schematic diagram of a conventional gamma camera used in SPECT [2]

1.3 Myocardial Perfusion Imaging

Myocardial perfusion imaging holds significant importance in diagnosing and making therapeutic decisions in cardiac disease. These tests, comprising a range of non-invasive imaging techniques, aid clinicians in evaluating blood flow to myocardial regions [8]. Gathering data on perfusion and metabolite uptake from the myocardium is crucial for determining optimal medical treatment or intervention strategies to enhance cardiac health [8]. These diagnostic tools serve various purposes across clinical scenarios, including evaluating symptoms suggestive of angina, excluding acute coronary syndrome as a cause of chest pain, assessing therapeutic efficacy post-

interventions, and identifying viable or scarred myocardium. By leveraging such insights, clinicians can comprehensively evaluate a patient's coronary health, stratify risk for future cardiovascular events, evaluate therapeutic responses to interventions addressing perfusion abnormalities, and provide prognostic information [8].

Perfusion imaging employs various radiotracers administered to the patient, allowing distribution across multiple tissues. These radiotracers emit photons detectable by a gamma camera, typically containing either a single NaI crystal for SPECT or multiple crystals, commonly used in PET, to interact with captured photons. Equipped with a collimator (physically in SPECT or electronically through coincidence detection in PET) to minimize background noise and a photomultiplier, these cameras convert photon-crystal interactions into electrical signals to generate images [8,9].

In SPECT imaging, prevalent radiotracers include thallium-201 or technetium-based compounds such as technetium-99m sestamibi or technetium-99m tetrofosmin. Thallium-201 actively distributes into myocardial cells, whereas technetium-based radiotracers passively rely on blood flow and myocardial viability for distribution. These radiotracers are administered during cardiac stress induced by exercise or pharmacological means. Uptake of the radiotracer indicates areas of perfusion and viable tissue during stress and at rest. Regions exhibiting poor perfusion during stress demonstrate improved perfusion at rest, termed reversible ischemia [8,9].

SPECT, widely utilized and accessible in contemporary clinical practice, employs planar images to reconstruct a three-dimensional depiction of myocardial perfusion. In contrast to planar imaging, SPECT can capture sequential slices without overlapping normal and abnormal regions, thereby enhancing resolution compared to planar imaging [8,10]. SPECT imaging has been validated through numerous large-scale studies for detecting coronary artery disease. Nevertheless,

this imaging modality does have some limitations [8,11,12]. These limitations encompass artifacts induced by factors like motion, attenuation, or extracardiac activity, which can impact the quality of images, along with variability among readers [8, 13]. Moreover, SPECT imaging commonly relies on technetium-99m tracers, which exhibit low first-pass extraction rates, consequently resulting in the underestimation of ischemic changes in both extent and severity [8,14].

A typical protocol for obtaining SPECT imaging to access myocardial perfusion and tissue viability are as follow [16]:

Technetium-99m (^{99m}Tc) one-day rest-stress imaging protocol [8]

1. ^{99m}Tc radiotracer is injected intravenously.
2. 30 to 60 minutes later, resting myocardial perfusion images are obtained.
3. Depending on availability and patient characteristics, a vasodilator (pharmacologic stress) is administered (either dipyridamole 0.56 mg/kg, adenosine 140 mcg/kg/min for a 6-minute infusion, or regadenoson 0.4 mg injection). A second dose of radiotracer is also administered.
4. 15 to 45 minutes later stress images are obtained.
5. Rest and stress images are ready for review and interpretation by a trained professional.

1.4 Cardiac-gated SPECT (C-SPECT)

Electrocardiogram (ECG) gated single-photon emission computed tomography (SPECT) myocardial perfusion imaging (MPI) is best recognized as a practical method for assessing left ventricular ejection fraction (EF) and volumes in addition to myocardium viability [17]. These measurements hold significant value in the care and monitoring of individuals with coronary artery disease (CAD) [17]. In the United States, an estimated 5 to 7 million SPECT MPI studies are conducted annually, with over 90% of them employing ECG-gated techniques, commonly known as Cardiac-gated SPECT (C-SPECT) [16]. In gated SPECT, data acquisition is segmented into

multiple time intervals of the cardiac cycle based on the ECG signal, and separate images are reconstructed for each of these intervals, also known as gates [30].

The advantages of ^{99m}Tc-labeled perfusion agents compared with the planar imaging and SPECT with ^{201}Tl are its ability to provide comprehensive information on regional and global left ventricular systolic function through ECG gating of images [19]. The superior quality of images obtained with these agents compared to ^{201}Tl is evident due to the more advantageous physical characteristics of ^{99m}Tc imaging with a gamma camera. With ^{99m}Tc, doses approximately 10 to 20 times higher than those feasible with ^{201}Tl can be administered, resulting in images with higher count density and fewer artifacts. Additionally, ^{99m}Tc demonstrates less scatter and attenuation than ^{201}Tl, which translates to reduced image artifacts, particularly in patients without CAD. Importantly, ^{99m}Tc -sestamibi or ^{99m}Tc -tetrofosmin imaging facilitates easy gated acquisition, allowing for the simultaneous assessment of regional systolic thickening, global left ventricular function, and myocardial perfusion [19,20].

ECG-gated SPECT provides crucial insights into global left ventricular function, previously requiring additional tests like radionuclide angiography, echocardiography, or contrast ventriculography [19,23,24]. The capacity to precisely measure left ventricular ejection fraction using ^{99m}Tc-sestamibi or ^{99m}Tc-tetrofosmin enhances the procedure's value, especially concerning prognostication and viability assessment [19]. With an analysis showing studies utilizing exercise ^{99m}Tc -sestamibi SPECT imaging revealed a sensitivity of 90% for ^{99m}Tc -sestamibi and 83% for ^{201}Tl in detecting CAD [25]. The specificity for SPECT ^{99m}Tc -sestamibi was 93%, compared to 80% for SPECT ^{201}Tl, with a normalcy rate of 100% for ^{99m}Tc -sestamibi and 77% for ^{201}Tl [25]. Overall, gated perfusion imaging notably enhances diagnostic accuracy for end-diastolic slices by producing higher-quality images [22].

1.5 Attenuation Correction in C-SPECT

Attenuation artifacts in C-SPECT image significantly contributed to the high false-positive rate [19]. Attenuation is caused by the gamma photons either scattered or photoelectric absorption, which never reach the detector. In particular with obese and women patients, distinguishing breast attenuation artifacts in women from perfusion abnormalities secondary to reversible ischemia or myocardial scar can be challenging at times [19]. Multiple studies have shown due to extraction being reduced, the ^{99m}Tc tracers is proportional to regional blood flow, showing a higher first pass myocardial extraction [19,21].

False-positive defects are frequently observed in the inferoapical region toward the basilar segment of the left ventricle [19]. In women, attenuation artifacts typically arise from overlying breast tissue, localized in the anterior wall and septum [19]. Additionally, a high diaphragm can induce attenuation artifacts in the inferior wall. Gated ^{99m}Tc perfusion imaging enables the assessment of systolic thickening from end diastole to end systole on SPECT tomograms [19]. Recognizing normal systolic thickening in a hypoperfused area directs the interpreter to conclude that a defect is an attenuation artifact rather than a myocardial scar, as the latter would likely exhibit reduced systolic thickening on gated tomograms [19]. A study has further proven and shown promising results of a same group of women, ^{99m}Tc -sestamibi SPECT perfusion imaging alone enhanced specificity to 84% [22]. Further analysis of gated images resulted in a specificity improvement for CAD detection to 92% [22]. Consequently, gated ^{99m}Tc-sestamibi imaging notably decreased the false-positive rate in these women from 33% with ^{201}Tl to just 8% [19, 22].

Apart from scatter and attenuation, SPECT MPI images also suffer from spatial blurring and patient motion. C-SPECT, with its division of the acquisition into multiple gates for each cardiac cycle, further exacerbates the challenge of noise [15]. Despite its numerous advantages, C-

SPECT still grapples with the persistent challenges of attenuation and motion, both significant contributors to artifacts that may lead to potential misdiagnosis [26].

A variety of image reconstruction techniques have emerged to address noise reduction in C-SPECT, including prefiltering, post-filtering, and advanced joint spatiotemporal 4D reconstruction methods, aimed at significantly improving image quality [27-30]. These methodologies integrate spatial and temporal data from gated frames, utilizing smoothing techniques within and across these frames [30]. Motion compensation spatiotemporal 4D reconstruction has demonstrated substantial enhancements in reconstruction precision and the ability to detect perfusion defects [30].

Besides noise reduction, it's essential to compensate for degradation factors, such as attenuation, scatter, and distance-dependent spatial resolution, in SPECT imaging as these factors may result in diminished contrast or false perfusion defects in the reconstructed images, compromising diagnostic accuracy and interpretation [31]. In clinical practice, attenuation correction (AC) is regularly carried out using integrated SPECT systems equipped with transmission tomographic imaging. There are two major methods to generate non-homogeneous attenuation maps for AC of SPECT: transmission-less and transmission-based scanning. The transmission-less method approach does not involve external scanning and is presumably less costly and complex [32] (the details about its implementation and effectiveness are beyond the scope of this work). The transmission-based scanning employs either an external radionuclide or X-ray computed tomography (CT) for imaging. Using hybrid SPECT/CT systems is highlighted as the most effective approach for generating non-homogeneous attenuation maps [32]. However, these systems are notably more expensive compared to SPECT-only systems [32]. They also require larger imaging housings and additional lead shielding, presumably due to the more

complex technology involved [32]. The prospective integration of low-dose cone-beam CT (CBCT) imaging presents exciting possibilities for SPECT MPI. This integration could potentially incorporate calcium scoring, provided that there are advancements in the image quality of CBCT. While diagnostic CT offers high-quality transmission images within a single breath-hold, it tends to introduce more artifacts compared to the slow CBCT acquisition, which can average patient respiratory motion similar to SPECT [33].

1.6 Dual Cardiac-respiratory Gated SPECT (D-SPECT)

SPECT MPI remains the preferred method for diagnosing coronary artery disease (CAD) in clinical practice [34, 35]. However, patient respiratory and cardiac motion during data acquisition often cause image blurring, compromising image quality, and potentially leading to diagnostic uncertainties in CAD interpretation [34]. Dual cardiac-respiratory gated SPECT (D-SPECT) has emerged as a solution to reduce both respiratory and cardiac motion blur simultaneously by sorting list mode data into different cardiac and respiratory gates based on motion information [36, 37, 38]. Due to each dual gate (DG) typically yields limited counts, resulting in higher noise levels [38].

Gated SPECT images, while effective for wall motion depiction, often exhibit increased noise due to reduced data counts within gate intervals. Numerous efforts in the literature aim to enhance gated image quality through spatiotemporal processing techniques, known as 4D methods. These include post-reconstruction spatiotemporal filtering [45], spatiotemporal regularization with a prior motion model [46], and simultaneous estimation of image motion and temporal regularization [47]. Additionally, a motion-compensated 4D reconstruction approach has been developed,

showcasing notable improvements in gated SPECT reconstruction accuracy and robustness, even with reduced imaging doses [48].

Apart from cardiac motion, respiratory motion artifacts also affect SPECT images, potentially impacting left ventricle functional analyses and myocardial perfusion assessments. Various approaches have been explored to mitigate respiratory motion effects in cardiac SPECT imaging. These include motion correction applied to projection data before image reconstruction [49,50], as well as respiratory binned imaging, where data acquisition occurs at reduced motion extents during different phases of respiratory cycles [40].

While cardiac gating and respiratory binning have been studied separately in SPECT imaging, addressing both cardiac and respiratory motion simultaneously presents challenges due to substantially reduced data counts. Some studies have attempted to integrate both gating and binning schemes concurrently. For instance, a clinical myocardial perfusion imaging study incorporated respiratory motion correction before image reconstruction, followed by cardiac contraction correction on the reconstructed images [51]. Another approach involved end-expiration respiratory gating alongside cardiac gating in a stationary SPECT system [52]. However, these methods may encounter elevated noise levels in conventional SPECT systems using rotating cameras. Furthermore, the attenuation correction of D-SPECT uses the attenuation map averaged over the respiratory cycle [30], which may introduce mismatched AC artifacts. We aim to investigate the motion-matched AC for D-SPECT in this work.

CHAPTER 2 NCAT Phantom Simulation

2.1 The 4D NURBS-based Cardiac-Torso (NCAT) Phantom

Computerized phantoms play a crucial role in medical imaging research, offering a means to simulate various patient anatomies for quantitative evaluation and improvement of imaging devices and techniques. However, for them to be effective research tools, they must be anatomically realistic. Two main categories of computerized phantoms exist: voxelized and mathematical. Voxelized phantoms, derived from segmented patient data, are highly realistic but limited in modeling anatomical variations and patient motion, requiring significant manual effort to create. Mathematical or stylized phantoms, defined mathematically using simple geometric primitives, offer flexibility in modeling variations and motion but lack realism [39].

The 4D NURBS-based cardiac-torso (NCAT) phantom is a sophisticated computerized dynamic torso model developed for medical imaging research [40]. It utilizes non-uniform rational B-splines (NURBS) to create realistic and flexible three-dimensional (3D) models of organ shapes based on human image data. Initially, the NCAT phantom focused on creating a realistic beating heart model, including coronary arteries, myocardial perfusion defects, and lesions. This was achieved by developing 4D NURBS cardiac models using gated magnetic resonance imaging (MRI) and tagged MRI data, allowing an accurate representation of cardiac motion and anatomy changes over time [40]. It features the addition of 3D NURBS models for the remaining torso organs and the incorporation of respiratory motion into the model. An interactive software application was developed to facilitate anatomical variations, allowing customization for different patient populations. The NCAT phantom was demonstrated to be useful in simulation studies for various medical imaging techniques, including SPECT, PET, and x-ray CT. Simulation studies using the NCAT phantom showed its effectiveness in reproducing physiological and physical

factors affecting medical imaging, such as cardiac and respiratory motion artifacts[40].

The NCAT phantom's organ models were crafted using cubic NURBS surfaces to authentically portray human torso organs. To convert these surfaces into a 3D image format, a common approach involves first triangulating the surface and then rendering the resulting triangles. Various algorithms exist for efficiently rendering triangles in computer graphics. NURBS surfaces are defined by two parametric variables, u and v, akin to latitude and longitude, respectively. An iterative subdivision method can generate triangles from the surface by traversing through u and v incrementally. However, determining the optimal step sizes for this method can be challenging and computationally expensive. Adaptive subdivision presents a superior alternative. This approach recursively subdivides the surface into smaller sections, stopping when a sub-surface is deemed flat enough to approximate with triangles. Adaptive subdivision minimizes unnecessary computation by ensuring that the generated triangles accurately represent flat portions of the surface, making it particularly suitable for Bezier surfaces due to their faster and more efficient subdivision compared to NURBS surfaces [40]. Bezier surfaces are utilized in computer graphics due to their exceptional properties[40]. These surfaces are described by a parametric equation, where n represents the surface's degree and $P_{i,j}$ are the control points. The Bezier basis functions, or blending functions, denoted as Bi,n and $B_{j,n}$, are defined using Bernstein polynomials. Bernstein polynomials are constructed with binomial coefficients. An illustration of a Bezier surface is depicted in Figure 5, showcasing a cubic Bezier surface formed by 16 control points arranged to approximate the surface's shape within a convex hull [40].

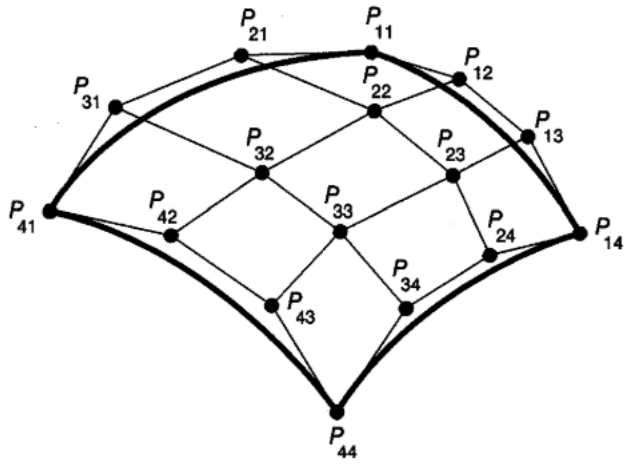

Figure 5. Cubic Bezier surface[40].

Bezier surfaces and NURBS surfaces share similarities in their representation with two parametric variables, control points, and blending functions. However, a notable difference lies in their flexibility and complexity. Bezier surfaces, defined by 16 control points, require joining multiple surfaces to form complex shapes, making them less flexible compared to NURBS surfaces. Converting NURBS surfaces to Bezier form is straightforward, achieved by decomposing the NURBS surface into multiple Bezier surfaces through the insertion of knots. This process results in a set of Bezier patches corresponding to the original NURBS surface[40]. The subdivision of Bezier surfaces is more straightforward and efficient compared to other representations, making them ideal for adaptive subdivision algorithms. This subdivision involves splitting the surface along one parameter, and then subdividing the resulting surfaces along the other parameter[40].

A software program has been developed to generate pixelized versions of the NCAT phantom using cubic Bezier surfaces and adaptive subdivisions. This program allows users to control the generation of activity or attenuation phantoms, providing a valuable tool for creating pixelized representations of the 4D NCAT phantom [40]. It requires NURBS surface definitions

for the organ models and a user-defined parameter file as input. The NURBS definitions for each organ of the torso are precompiled into one text file for the program. After reading the NURBS organ models and the user-defined parameter file, the NCAT program modifies the organ models accordingly[40]. Once the NURBS organ models are modified, each cubic NURBS organ model is decomposed into cubic Bezier surfaces. These surfaces are then subjected to an adaptive subdivision algorithm to accurately approximate the organ models with triangles. The algorithm prioritizes rendering organs to handle overlapping surfaces, and surfaces are tested for flatness before subdivision. If a surface fails the flatness test, it is subdivided further until all Bezier surfaces defining the organ are converted into triangles [40]. Once an organ is approximated with triangles, they are rendered into a 3D image format by intersecting each triangle with defined slice planes. The intersection of a triangle with a slice plane corresponds to a line on the plane, which is found by intersecting each edge of the triangle with the slice plane. Each edge of the triangle is parametrically defined, and intersections are calculated by substituting the slice plane value into the parametric equations. If an intersection is found, it forms a line on the slice plane, and this process is repeated for each triangle and slice plane[40].

After all triangles defining an organ surface are rendered, each slice plane containing the organ surface is filled using a scanline routine to create a solid representation. This routine searches each line in each slice plane for edges and fills in between them to form a solid. The bounding box for each organ is used to limit the search area for efficiency. The filled organ is assigned an intensity value based on the user-defined parameter file. In an activity phantom, organs are filled with their relative radioactivity concentrations, while in an attenuation phantom, organs are filled with their respective attenuation coefficients. Thoracic tissues are classified into muscle, fat, soft tissue, lung, spinal bone, and rib bone, and their attenuation coefficients are calculated accordingly

[40]. Two sets of 3D pixelized phantoms are generated representing distributions of attenuation coefficients and radioactivity concentrations in organs. The scan conversion routine prioritizes rendering the current organ, ignoring previously rendered organs except for overlap, which is refilled with the intensity of the current organ. This priority system ensures an accurate representation of organ layers in the final image[40].

The new 4D NCAT phantom offers improved realism in modeling human anatomy and motions compared to its predecessor. Patient motions are simulated by transforming the control points of NURBS organ models. For instance, to mimic upward creep motion, the heart and diaphragm are initially translated downward by 2 cm and then moved upward at a constant velocity during data acquisition, representing the return of the heart to its resting position.

Respiratory motion involves up-and-down movement of the diaphragm and tilting of the ribcage. The heart moves with the diaphragm, and the lungs expand and contract with changes in thoracic cavity volume due to rib movements. The respiratory motion is modeled sinusoidally over 2 cm to simulate normal tidal breathing [40]. Upward creep data are generated with 32 phantom sets, incrementally increasing diaphragm height. Respiratory motion data are generated with 20 phantom sets, with diaphragm movement averaged for upward and downward positions.

2.2 Generation of Activity Maps and Attenuation Maps for D-SPECT

The NCAT phantom can generate voxelized phantoms with the following specific binary or text files:

1. **dncat_bin**: Produces voxelized phantoms from a parameter file, saving them as raw binary files. It generates phantoms with either activity or attenuation coefficients, based on the

parameter file. A sample parameter file is provided with the software.

2. **hrt_lesn_bin**: Specifically generates voxelized activity phantoms of left ventricle (LV) perfusion defects. It models perfusion defects as pie-shaped wedges in the LV myocardium. Requires the use of **dncat_bin** to generate original heart phantoms.
3. **dplaq_bin**: Used for modeling plaques in the aorta or coronary arteries. Generates voxelized activity or attenuation phantoms of cardiac plaques modeled as NURBS surfaces inside the selected vessel.
4. **lesn_bin**: Models spherical lesions in the lungs or liver. Generates voxelized activity or attenuation phantoms of lesions modeled as simple spheres. Requires **dncat_bin** to generate original phantoms.
5. **hrt_vectors** and **resp_vectors**: Outputs motion vectors for the beating heart and respiratory motion (lungs, liver, diaphragm, and non-beating heart), respectively. These programs do not produce phantom images but only output motion vectors as text files.

For this research, we will first use dncat_bin to generate the original heart phantoms, then use the hrt_lesn_bin to generate voxelized activity phantoms of left ventricle (LV) perfusion defects. It models perfusion defects as pie-shaped wedges in the LV myocardium.

We adjusted the parameter file to represent a female anatomy with the following parameters: body long axis defined as 33 cm, body short axis as 25 cm, rib long axis as 28 cm, rib short axis as 21 cm, height as 188 cm, weight as 86 kg, breast long axis as 18.2 cm, breast short axis as 7 cm, breast height as 14 cm. Additionally, we set the pixel width, slice thickness, and array size to 0.634 cm, 0.634 cm, and 64. The dimensions of the NCAT phantom were 64×64×64 with a voxel size of $6.34 \times 6.34 \times 6.34$ mm^3.

An NCAT female phantom (a defect absent phantom (DAP) [40] with cardiac motion (8

phases) and respiratory motion (8 phases) was used to compare the performance of averaged and motion-matched AC. After we generated the activity maps and attenuation maps, we used ITK-SNAP software to view the three orthogonal slices of the acitivity maps of Tc-Sestamibi overlaid on the attenuation maps. Figures 6-8 show the ideal female phantom served as the ground truth. Figure 6 shows the axial plane, which divides the body into top and bottom sections. Figure 7 shows the coronal plane, which divides the body into dorsal and ventral sections. And Figure 8 shows the sagittal plane, which divides the body into right and left sections.

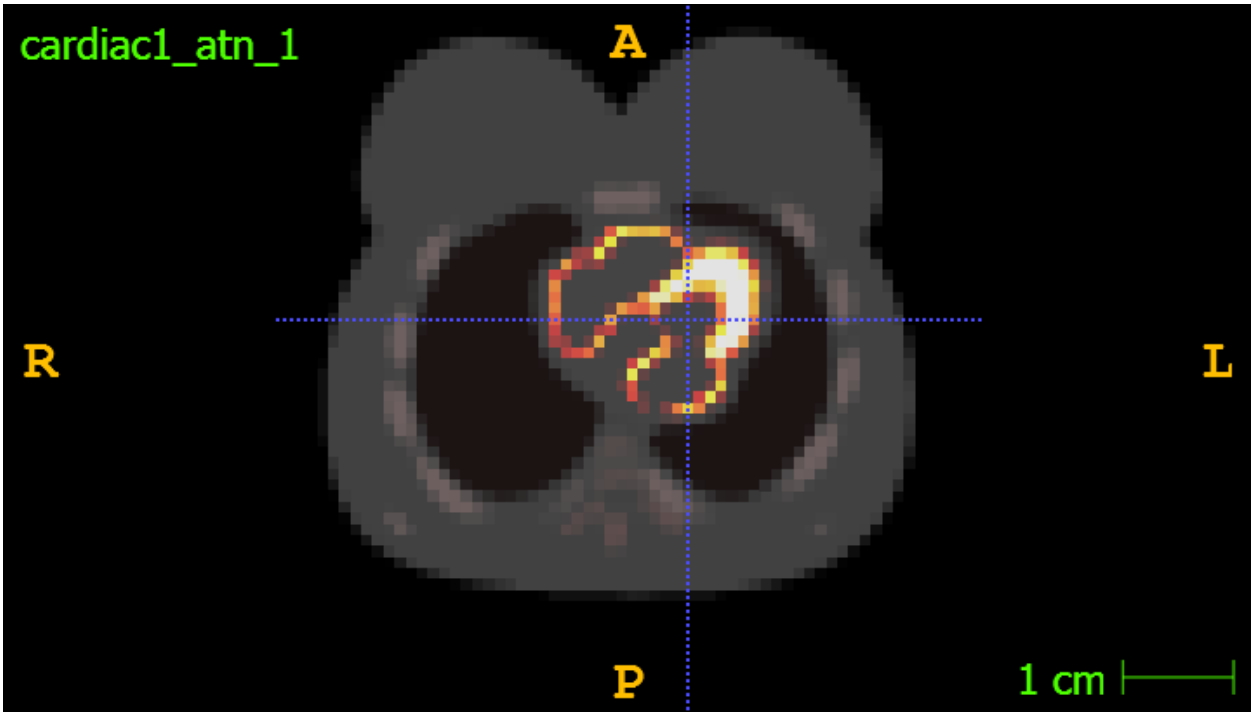

Figure 6. Axial plane view for the ideal female phantom: the activity map overlaid on the attenuation map.

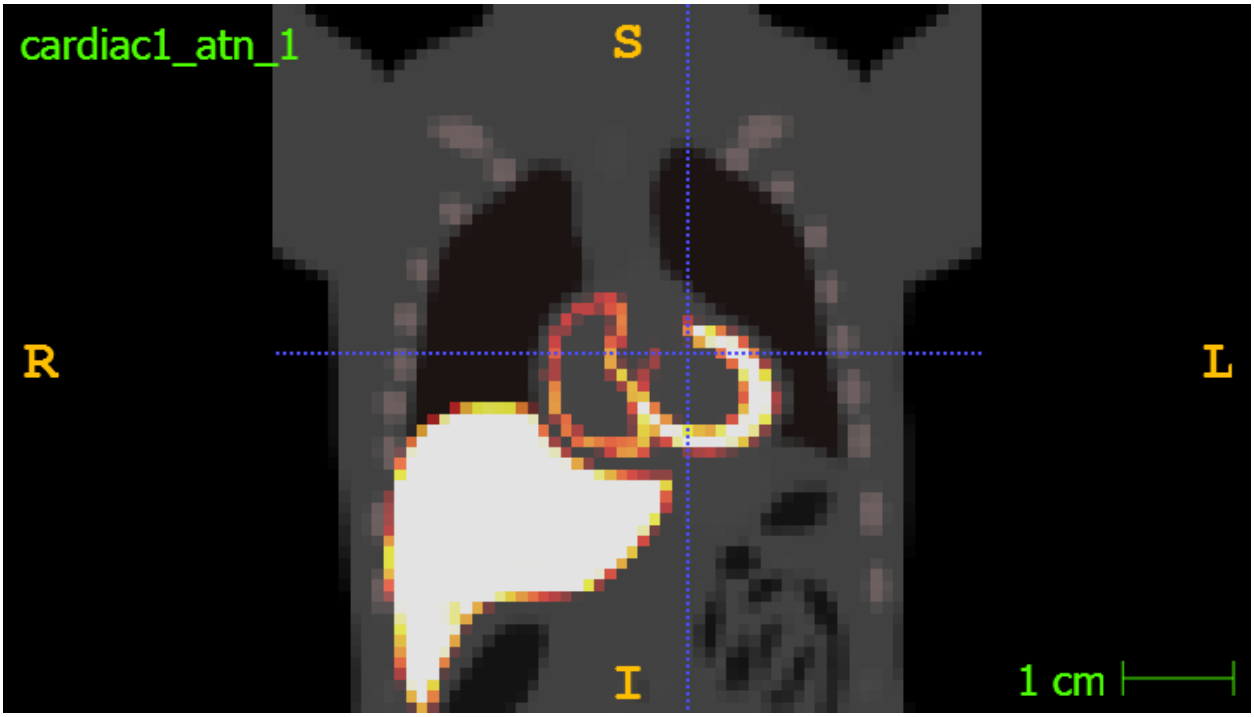

Figure 7. Coronal plane view for the ideal female phantom: the activity map overlaid on the attenuation map.

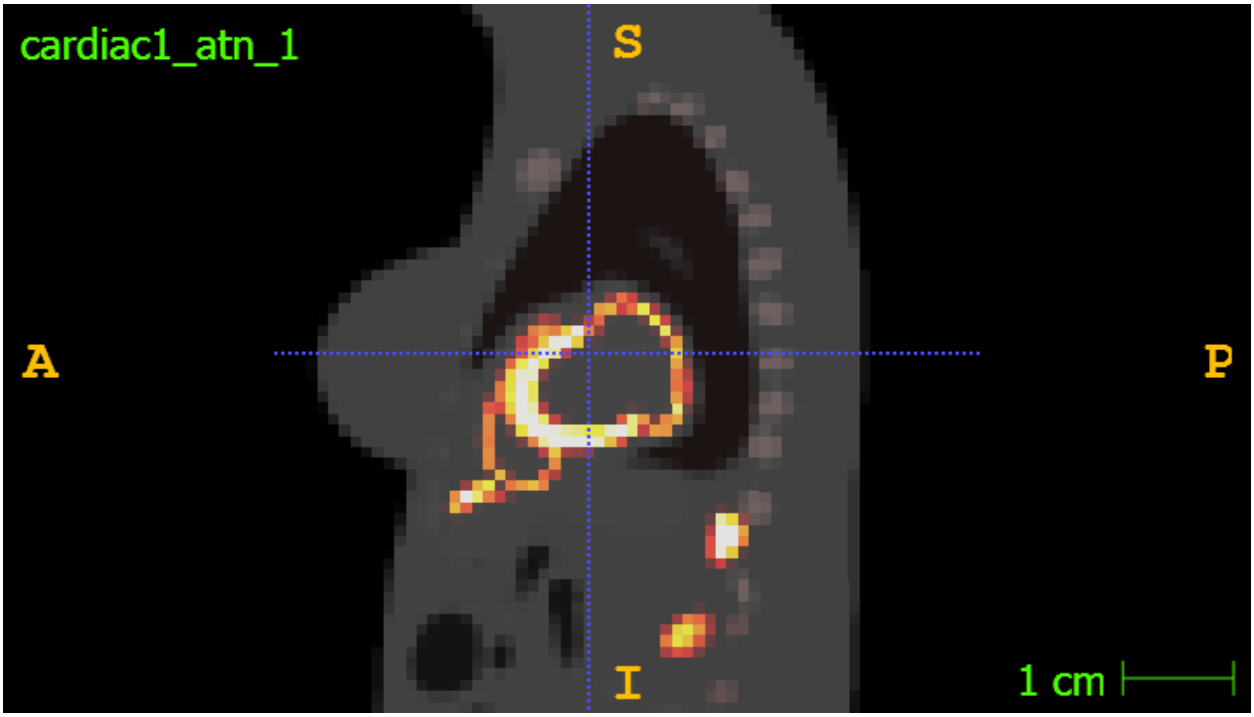

Figure 8. Sagittal plane view for the ideal female phantom: the activity map overlaid on the attenuation map.

2.3 Generation of Perfusion Defects

For this research, we defined four different cases based on the location of the lesion center in the circumferential dimension of the heart. In the first female case, as shown in Figure 9-11, the lesion was placed at the anterior wall with a theta center at 0 degrees (a parameter in the NCAT parametric input file). In the second female case, as shown in Figure 12-14, the lesion was placed at the inferior wall with a theta center at 180 degrees. For the third female case as shown in Figure 15-17, the lesion was placed at the lateral wall with a theta center at 90 degrees, while in the fourth female case, as shown in Figure 18-20, the lesion was placed at the septal wall with a theta center at 270 degrees. After generating the perfusion defect, it can be scaled and subtracted from the DAP to obtain the Defect Present Phantom (DPP), where the radioactivity was reduced by 20%.

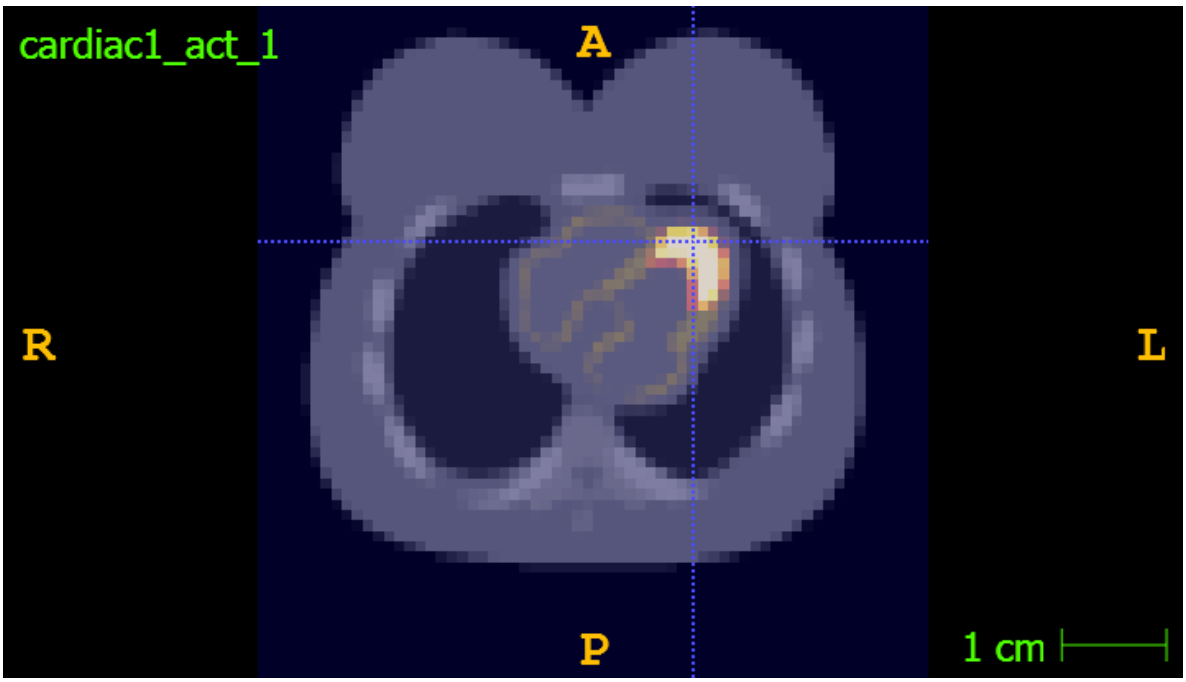

Figure 9. Axial plane view for the female case lesion at the anterior wall with a theta center at 0 degrees

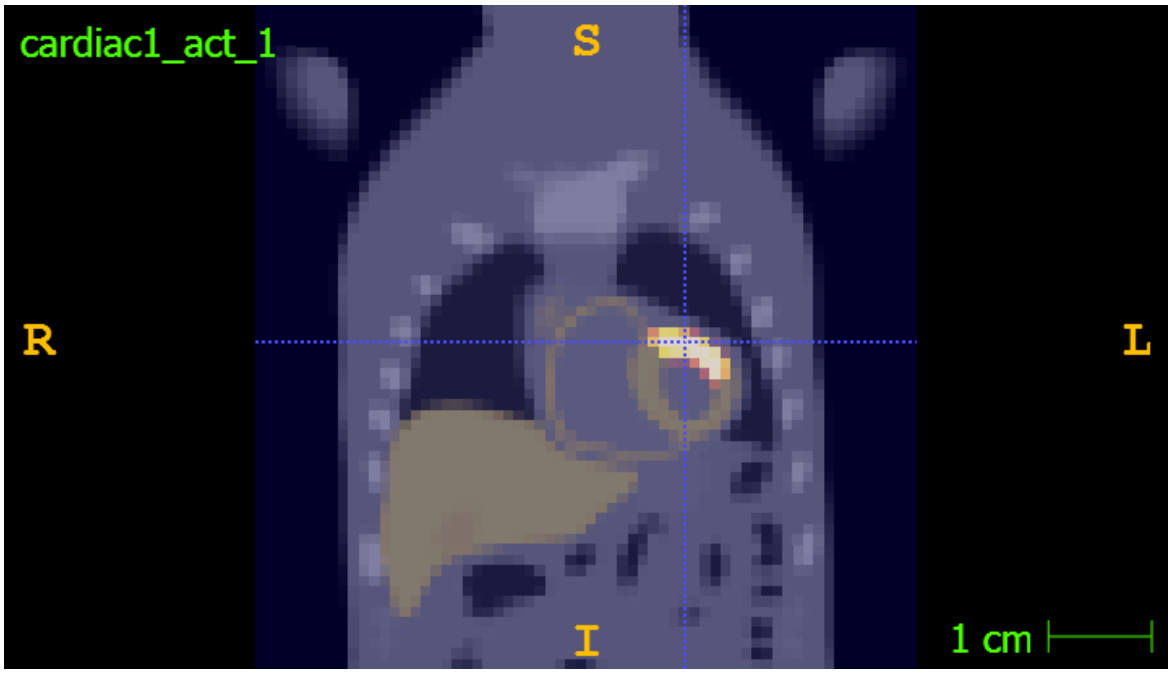

Figure 10. Coronal plane view for the female case lesion at the anterior wall with a theta center at 0 degrees

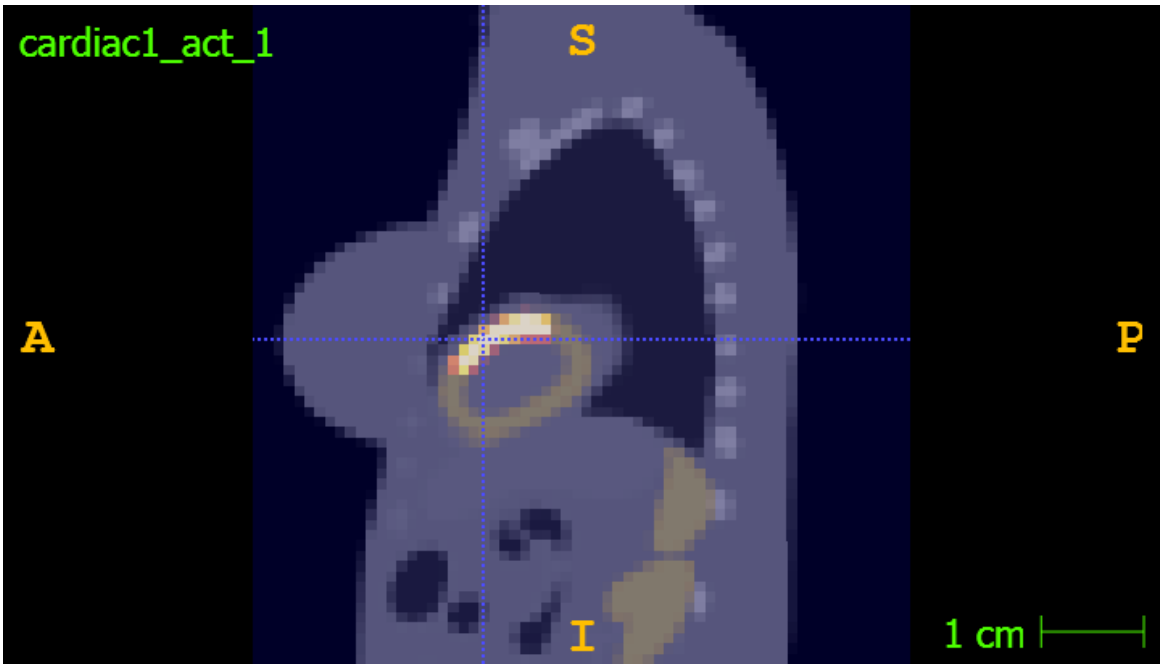

Figure 11. Sagittal plane view for the female case lesion at the anterior wall with a theta center at 0 degrees

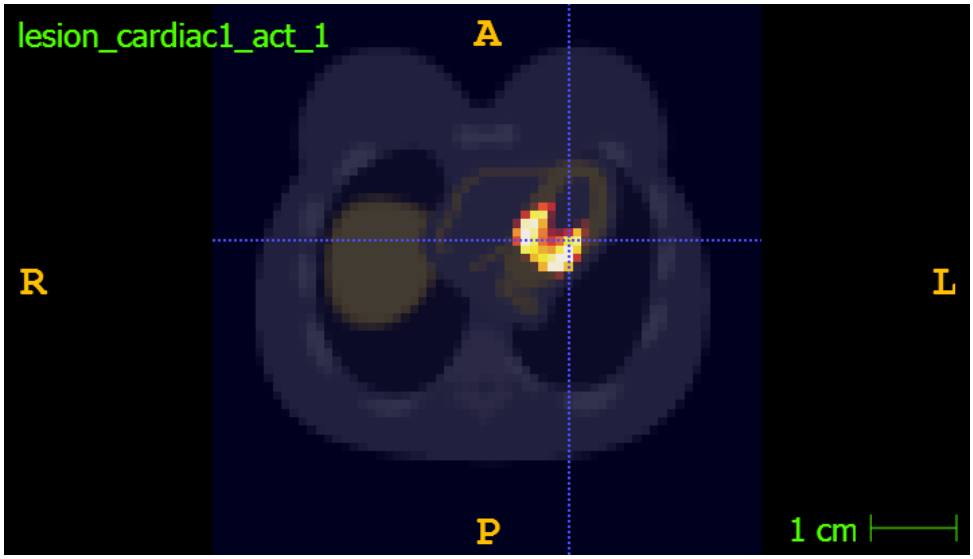

Figure 12. Axial plane view for the female case lesion at the inferior wall with a theta center at 180 degrees

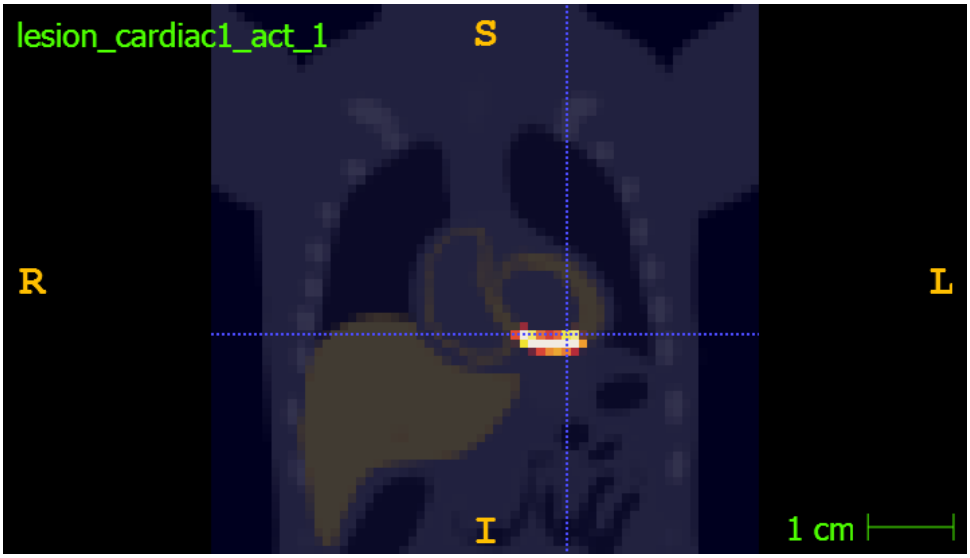

Figure 13. Coronal plane view for the female case lesion at the inferior wall with a theta center at 180 degrees

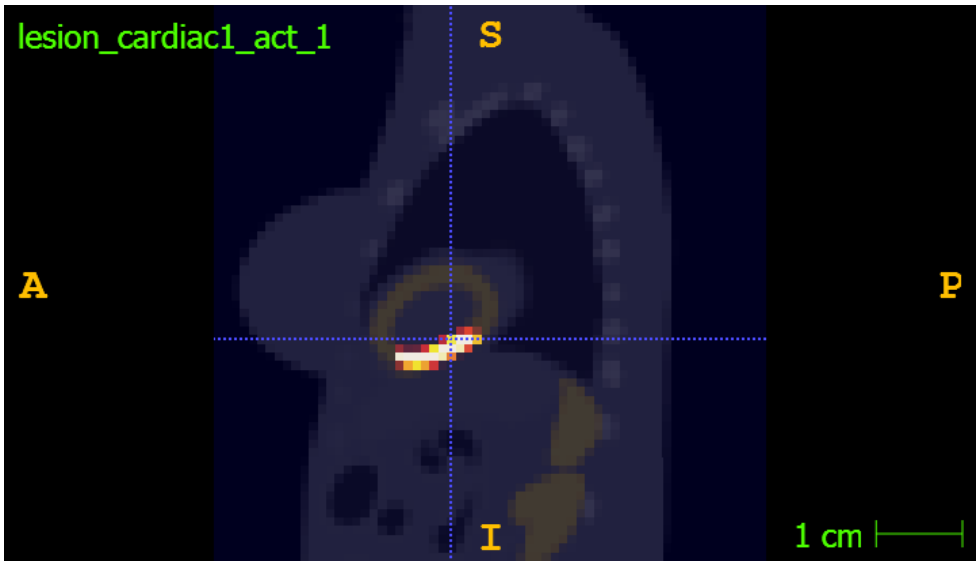

Figure 14. Sagittal plane view for the female case lesion at the inferior wall with a theta center at 180 degrees

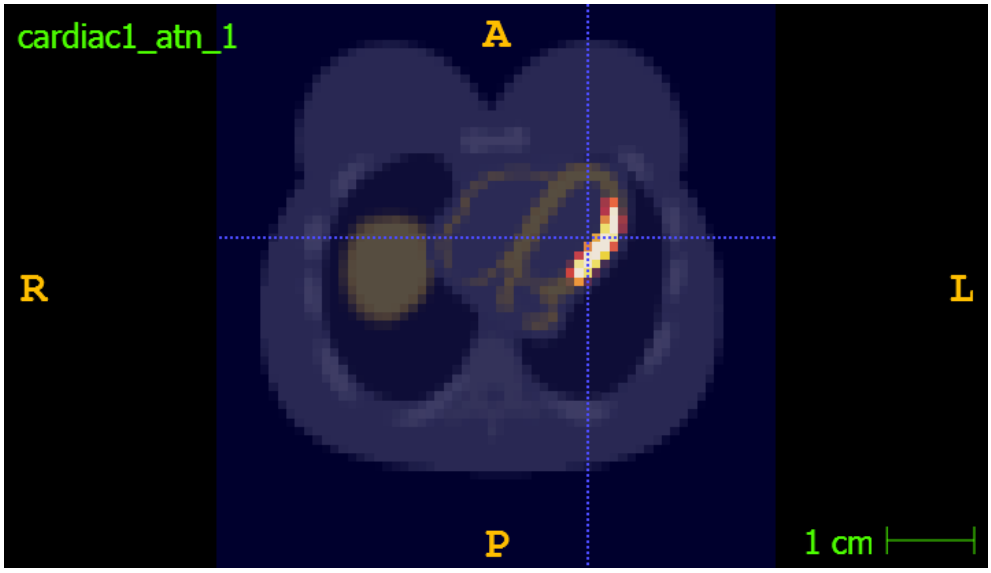

Figure 15. Axial plane view for the female case lesion at the lateral wall with a theta center at 90 degrees

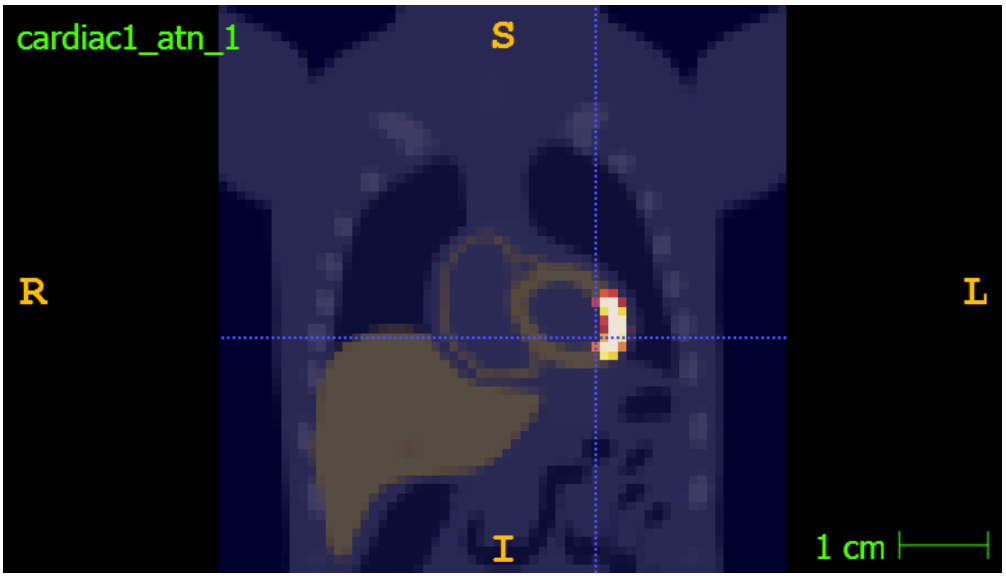

Figure 16. Coronal plane view for the female case lesion at the lateral wall with a theta center at 90 degrees

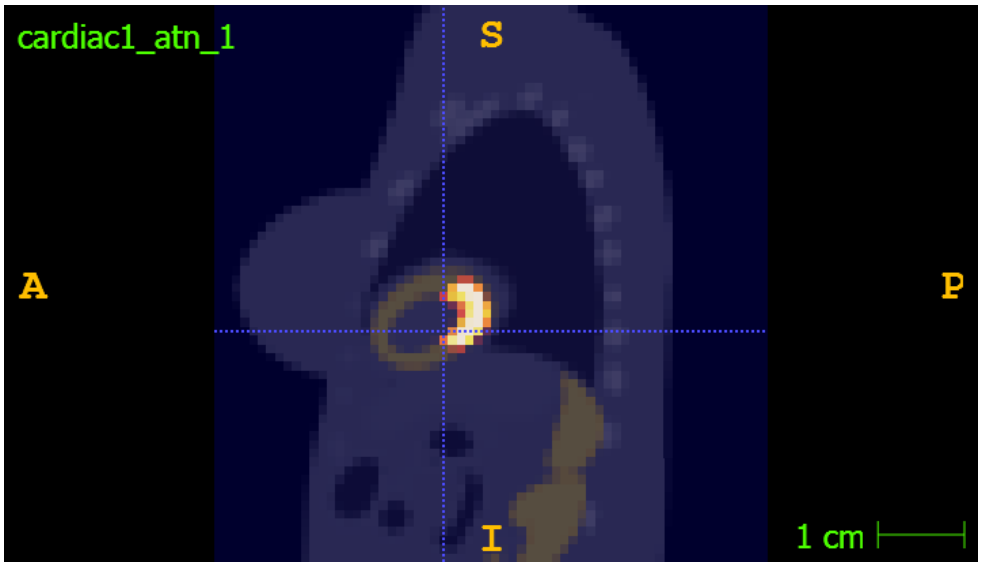

Figure 17. Sagittal plane view for the female case lesion at the lateral wall with a theta center at 90 degrees

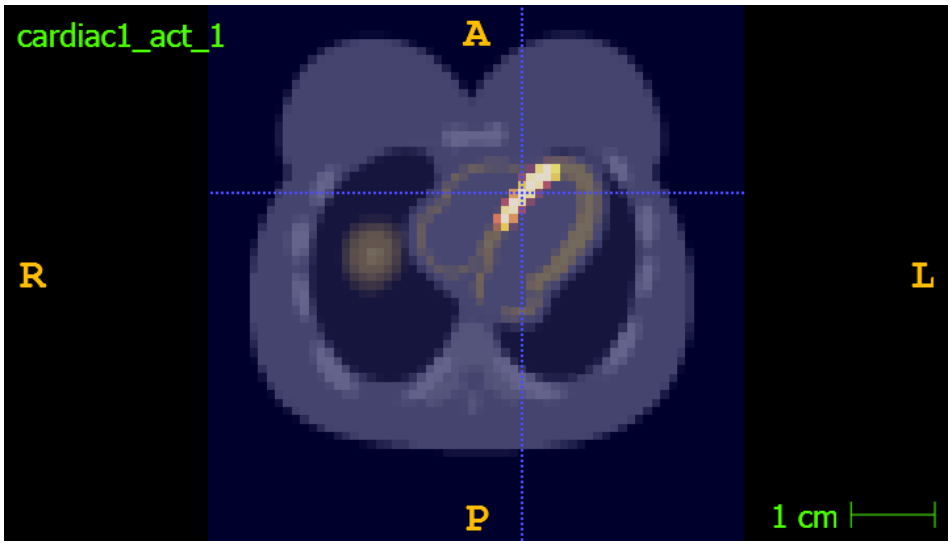

Figure 18. Axial plane view for the female case lesion at the septal wall with a theta center at 270 degrees.

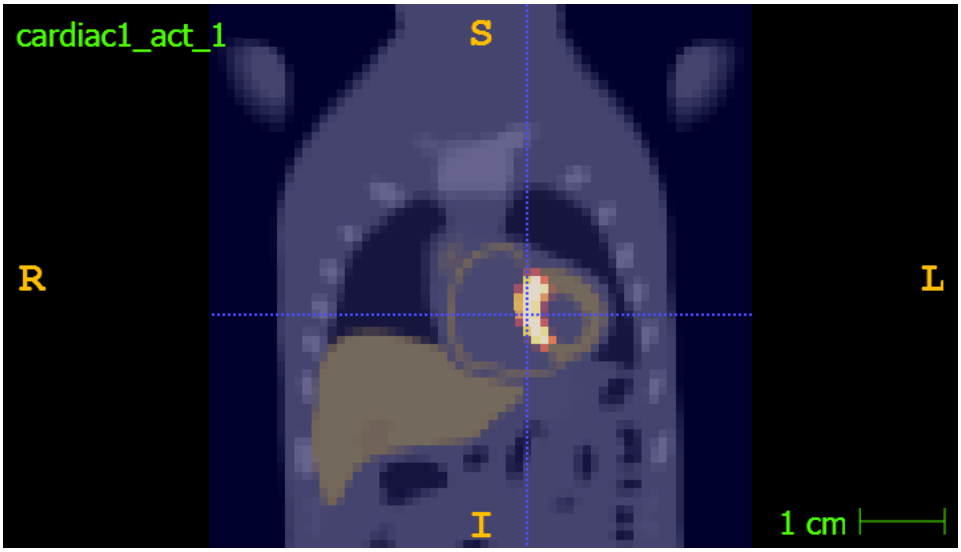

Figure 19. Coronal plane view for the female case lesion at the septal wall with a theta center at 270 degrees.

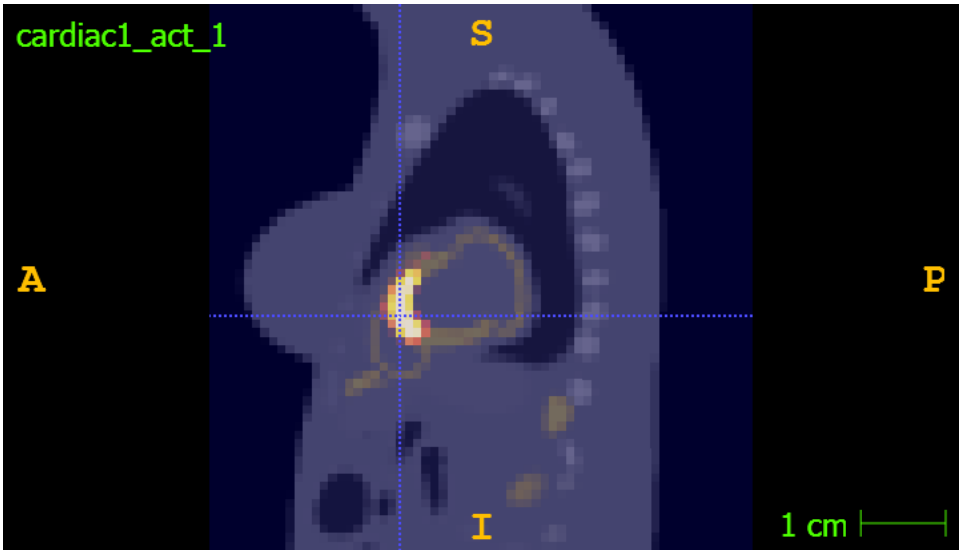

Figure 20. Sagittal plane view for the female case lesion at the septal wall with a theta center at 270 degrees.

CHAPTER 3 D-SPECT Simulation and Reconstruction with Different AC

3.1 Monte Carlo Simulation of D-SPECT

Monte Carlo Simulation is an important tool in medical imaging research. With its ability to replicate complex radiation processes within the human body, this simulation technique offers insights into the performance and optimization of SPECT imaging systems tailored specifically for cardiac examinations. By employing methods to model photon interactions and their subsequent detection, Monte Carlo simulations enable researchers to comprehensively evaluate imaging protocols, instrument design, and reconstruction algorithms with a high degree of precision. In this research, we used SIMIND was used to simulate D-SPECT imaging of ^{99m}Tc-Sestamibi [41] with the 4D NCAT phantom, which produces imaging data that closely resemble real patient data, providing a known ground truth for objective performance evaluation.

In many Monte Carlo applications, physical processes can be accurately simulated directly from known probability density functions (pdfs) [41]. By sampling from these pdfs, simulations can generate realistic data, requiring a large number of simulated histories to ensure accurate parameter estimation and minimize statistical errors[41]. Simulation studies offer advantages over experimental studies, allowing easy parameter manipulation to optimize system performance [41]. Early Monte Carlo studies, such as Anger and Davis's investigation of NaI(Tl) crystals, demonstrate the technique's utility in evaluating intrinsic efficiency and spatial resolution [41]. Additionally, Monte Carlo simulations enable the study of other parameters, like scatter components, contributing to a comprehensive understanding of radiation processes and imaging system performance[41].

3.2 The SIMIND Monte Carlo Program

SIMIND, a Monte Carlo code for simulating clinical SPECT scintillation cameras, offers SPECT imaging calculations and measurements [41]. It comprises two main programs, CHANGE and SIMIND, which facilitate easy customization and simulation [41]. The CHANGE program allows users to define simulation parameters through a menu-driven interface and write them to an external file [41]. SIMIND conducts the Monte Carlo simulations by reading input data from files generated by CHANGE, performing calculations, and outputting results to the screen or data files [41]. This approach enables the preparation of multiple input files in a command file for efficient batch processing and streamlining the workflow for Monte Carlo simulations [41]. Figure 21 shows a flowchart explaining the input and output files used and created by the SIMIND code [41].

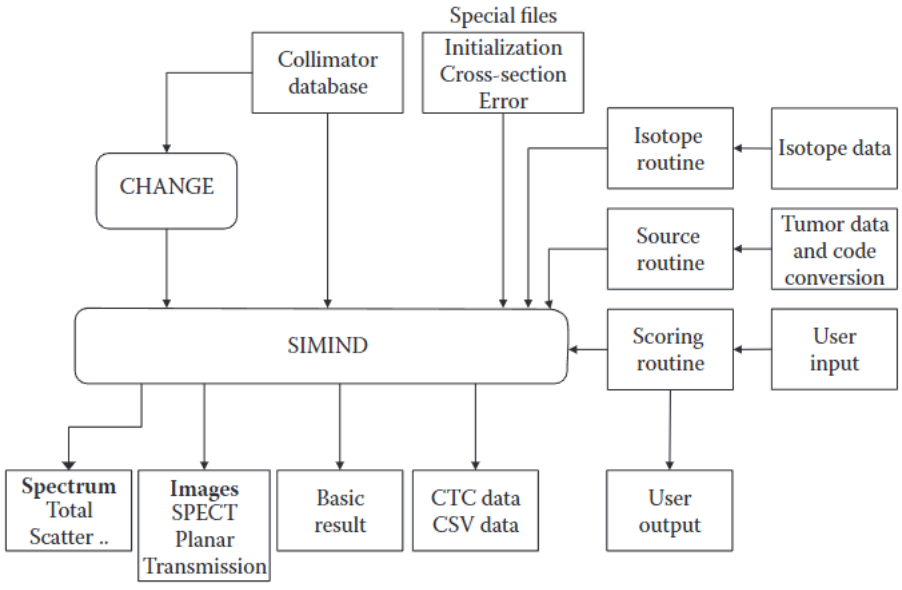

Figure 21. Flowchart of the input and output files used and created by the SIMIND code [41].

3.3 D-SPECT Imaging Model

In dual-gated imaging, projections are synchronized with both respiratory and cardiac motion. The description of these projections can be expressed using the following equation [30],

$$\boldsymbol{P}_{r,k} = \boldsymbol{H}\boldsymbol{I}_{r,k} + \boldsymbol{n}_{r,k}, k = 1, \dots, K, r = 1, \dots, R \quad , \qquad (1)$$

where $\boldsymbol{P}_{r,k}$ and $\boldsymbol{I}_{r,k}$ are representing the projection data and image data for the respiratory gate r and cardiac gate k. R and K are the number of gates for a respiratory or cardiac cycle, respectively (R= 8 and K = 8 in this work). $\boldsymbol{H}$ is the system matrix for the projection operation, consistently incorporating depth-dependent blur. Attenuation effects are also accounted in H for using either an average attenuation map or a respiratory motion-matched attenuation map.

In C-SPECT, when focusing only on cardiac motion, the reconstruction benefits from a relatively large photon count. Specifically, for each k, all R respiratory phases can be utilized. However, in D-SPECT, where both cardiac and respiratory motions are considered, the photon count significantly diminishes. In this scenario, only one respiratory phase, denoted as r, can be employed for each k. Let each D-SPECT projection be characterized as follows:

$$\boldsymbol{P}_{r=1,k=1}, \boldsymbol{P}_{r=2,k=1}, \dots, \boldsymbol{P}_{r=R,k=1}, \boldsymbol{P}_{r=1,k=2}, \boldsymbol{P}_{r=2,k=2}, \dots, \boldsymbol{P}_{r=R,k=2}, \dots, \boldsymbol{P}_{r=1,k=K}, \boldsymbol{P}_{r=2,k=K}, \dots, \boldsymbol{P}_{r=R,k=K}$$

And each C-SPECT projection be characterized as follows :

$$\boldsymbol{P}_{k=1} = \boldsymbol{P}_{k=1,r=1} + \boldsymbol{P}_{k=1,r=2} + \dots + \boldsymbol{P}_{k=1,r=R},$$

To explore motion-matched attenuation correction (AC) for dual-gated SPECT, we incorporate an attenuation map $\boldsymbol{Att}_r$ within system matrix H for each respiratory phase r. Conversely, for averaged AC, H contains the same attenuation map $\boldsymbol{Att}_{avg}$ applied across all respiratory phases.

As photons are distributed across various respiratory phases, the noise level significantly increases in each individually reconstructed cardiac-respiratory phase. To mitigate this noise, we

adopted the following comprehensive 4D reconstruction approach by leveraging information from all cardiac-respiratory phases.

3.4 4D Reconstruction for C-SPECT

Before D-SPECT reconstruction, we reconstructed all cardiac gates with a fixed respiratory phase, a methodology known as 4D C-SPECT reconstruction. This approach allows for a comprehensive examination of cardiac dynamics while considering respiratory motion. For reconstruction, two attenuation methods were compared in this research, the first method is the 4D reconstruction with an attenuation map averaged over all respiratory gates (AVE-AC); the second method is 4D reconstruction with an attenuation map of respiratory motion matched with the SPECT image (RMM-AC). The schematic representation of this process is illustrated in Figure 22, the framework for 4D reconstruction incorporating both averaged and matched attenuation correction (AC).

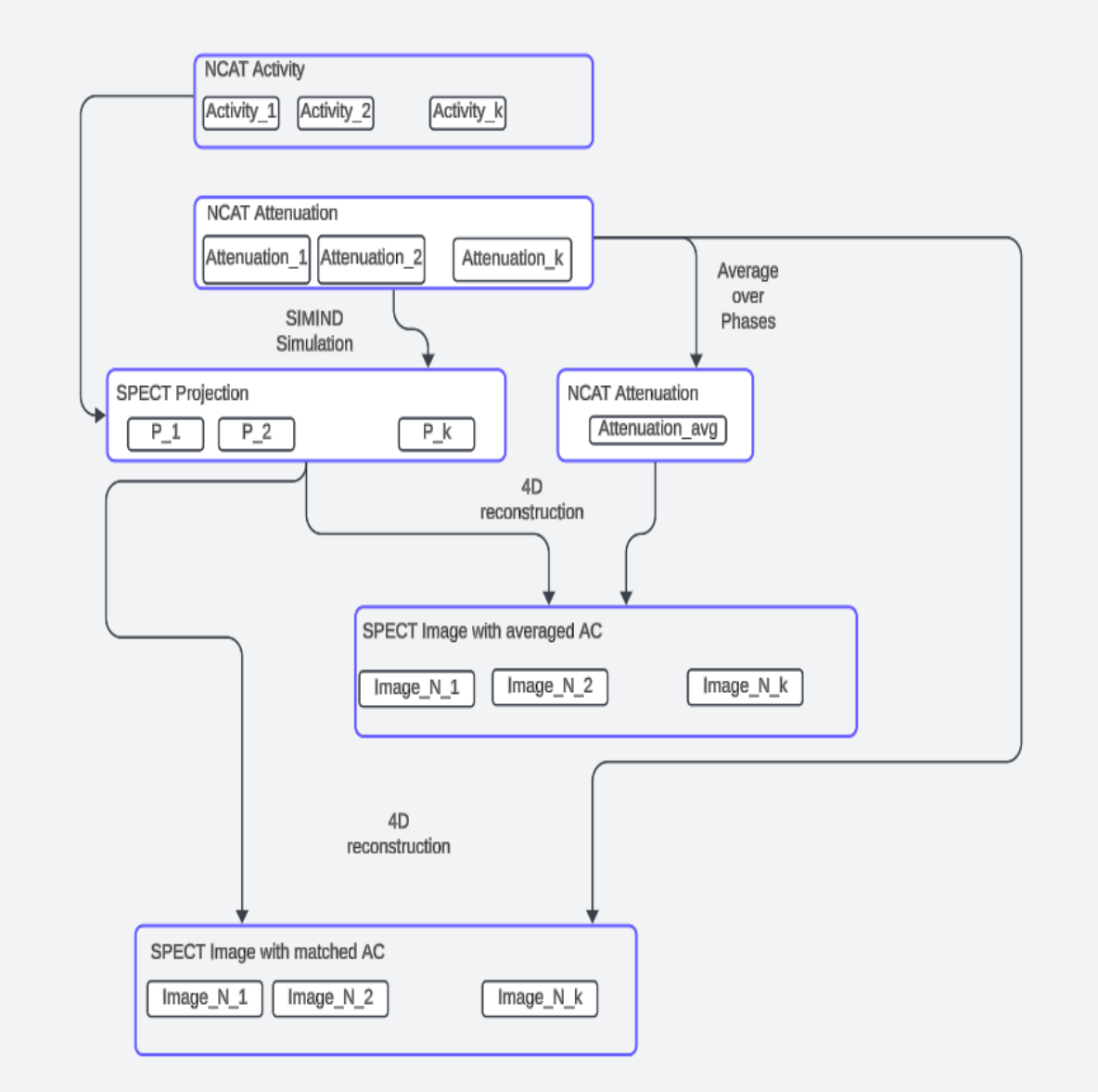

Figure 22. RMM-AC and AVE-AC for 4D Reconstruction

3.5 Post Reconstruction Respiratory Motion-compensated Smoothing for D-SPECT

Once we obtained images capturing all cardiac gates through the 4D reconstruction of C-SPECT for each respiratory gate, we aggregated images across all K cardiac phases to mitigate the photon noise as shown in the following equation, where i denotes the i-th respiratory phase and k denotes the k-th cardiac phase.

$$Img_i = \sum_{k=1}^{K} Img_{i,k} \quad (2)$$

Afterward, we proceed to estimate respiratory motion, specifically the deformation vector field (DVF), spanning from respiratory phases i to respiratory phase j utilizing the following equation:

$$DVF_{j\leftarrow i} = \frac{(Img_j - Img_i)\vec{\nabla} Img_i}{(\vec{\nabla} Img_i)^2 + (Img_j - Img_i)^2} \quad \text{for i=1, 2,…R and j=1, 2, …,R.} \quad (3)$$

When i= j, the deformation vector field (DVF) consists entirely of zeros. Utilizing DVF derived from Eq. (3), we can generate a warped image $\widetilde{Img}_{j\leftarrow i,k}$ at respiratory phase j from the image $Img_{i,k}$ at respiratory phase i, for a given fixed cardiac phase k.

$$\widetilde{Img}_{j\leftarrow i,k} = Imwrap\left(Img_{i,k}, DVF_{j\leftarrow i}\right). \quad (4)$$

To denoise the image at respiratory phase j and cardiac phase k, we aggregate all other respiratory phases. Given the higher accuracy of DVFs for adjacent phases, we employ a weighted sum to obtain the final respiratory motion-compensated temporally filtered image $\widehat{Img}_{j,k}$ outlined as follows:

$$\widehat{Img}_{j,k} = \sum_{i=1}^{R} \left|1 - 2 * \frac{|i-j|}{R}\right| * \widetilde{Img}_{j\leftarrow i,k} \quad (5)$$

These steps for post-reconstruction respiratory motion-compensated temporal smoothing in D-SPECT are illustrated in Figure 23.

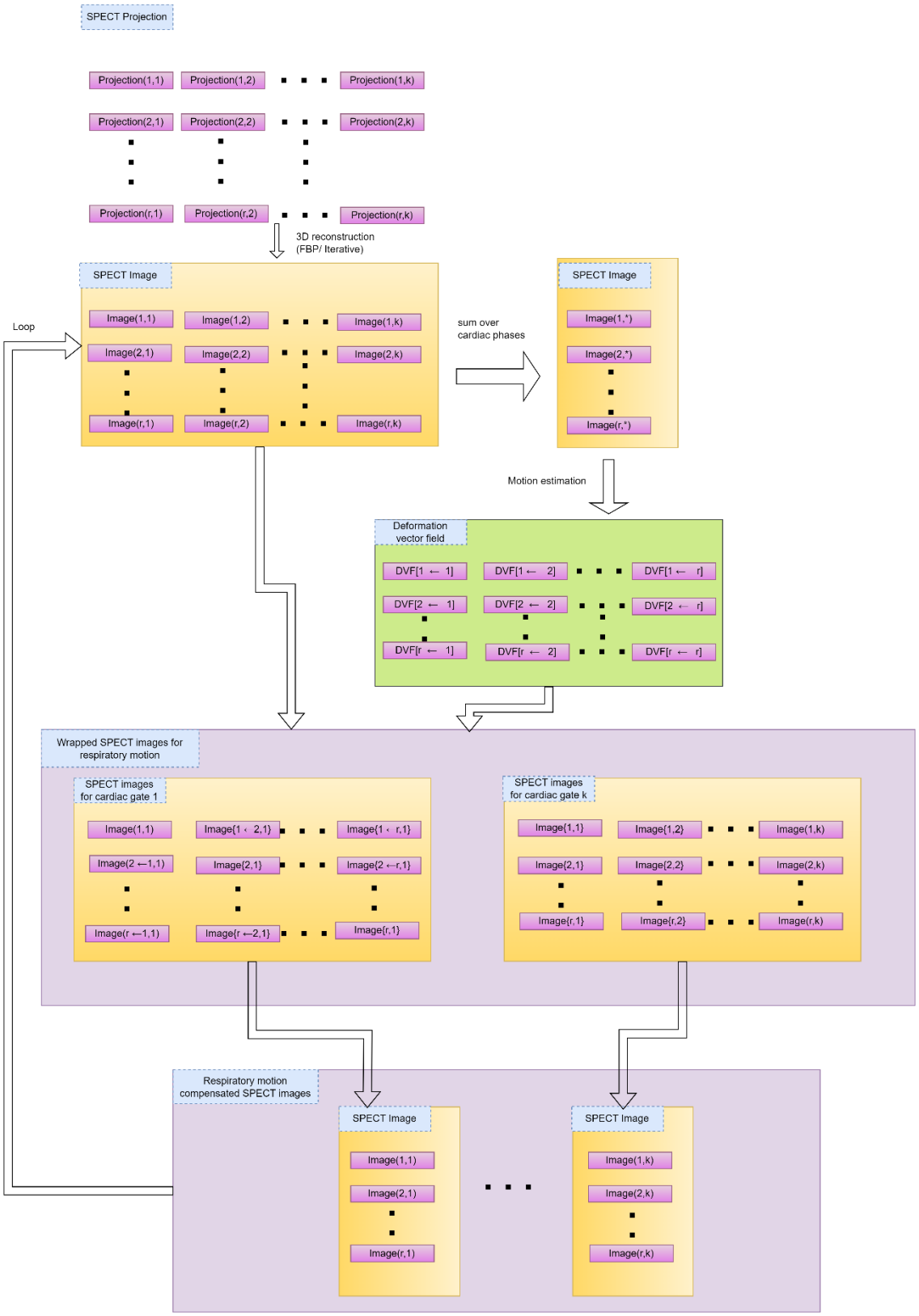

Figure 23. Post-recon respiratory motion-compensated smoothing for D-SPECT

3.6 Simulation study setup

We utilized a NURBS-based cardiac-torso (NCAT) phantom [40], incorporating both cardiac motion (8 gates) and respiratory motion (8 gates), to evaluate the performance of the respiratory motion-matched attenuation correction (RMM-AC) and attenuation map averaged over all respiratory gates (AVE-AC). The NCAT phantom dimensions were 64×64×64 with a voxel size of 6.34×6.34×6.34 mm^3. SIMIND was used to simulate D-SPECT cardiac perfusion imaging of ^{99m}Tc-Sestamibi [30]. To introduce realistic noise, Poisson counting noise of $1x10^6$ photons per respiratory phase was incorporated, resulting in only 125 thousand photons per respiratory and cardiac phase. The ground truth for evaluation was established through ideal reconstruction without the presence of noise, attenuation, and scatter in SIMIND simulation.

In order to assess the effectiveness of each method in detecting lesions, we introduced a lesion 60 mm with a 20% radiotracer concentration reduction in the left ventricular myocardium. To explore the influence of different AC methods on different lesion locations, we chose four lesion locations listed in Table 1 (also shown in Chapter 2).

Table 1. The lesion locations for four cases

	Case1	**Case2**	**Case3**	**Case4**
NCAT theta center(degree)	0	180	90	270
Location	Anterior	Inferior	Lateral	Septal

For reconstruction, two methods were compared in this research, the first method is the 4D reconstruction with an attenuation map averaged over all respiratory gates (AVE-AC); the second method is 4D reconstruction with an attenuation map of respiratory motion matched with the SPECT image (RMM-AC).

To assess the efficacy of the two methods, we used two metrics: the root mean squared error (RMSE) of reconstructed images and the area under the receiver operating characteristic (ROC) curve (Az) of the Channelized Hotelling Observer (CHO) for lesion detectability [42]. The RMSE is a performance indicator for a regression model. It measures the average difference between values predicted by a model and the actual values. In our research, the idea reconstruction of noiseless without attenuation and scatter serves as the ground truth for RMSE calculation. The CHO has been widely used as a surrogate for human observers in evaluating lesion detectability [43]. Az provides an estimation of how well an observer is able to detect the lesion.

CHAPTER 4 Results and Discussion

We use a clinical program called Cardiac Suite (CSImport) to validate the lesion locations as specified by the NCAT phantom. We developed an in-house MATLAB program to adjust the orientation of the heart appropriately to be imported into CSImport. Subsequently, the adjusted DPP images were imported into the CSImport to visualize the lesions' locations on the left ventricular (LV) segment across three cardiac planes. The ideal reconstruction without lesion and with lesions at four locations are in Figure 24 as heart short-axis images. The lesions are positioned in the north (anterior), south (inferior), east (lateral), and west (septal) directions of the heart wall with about 20% reduction in uptake intensity.

Without Lesion With Lesion $\Theta = 0^{\circ}$ With Lesion $\Theta = 180^{\circ}$

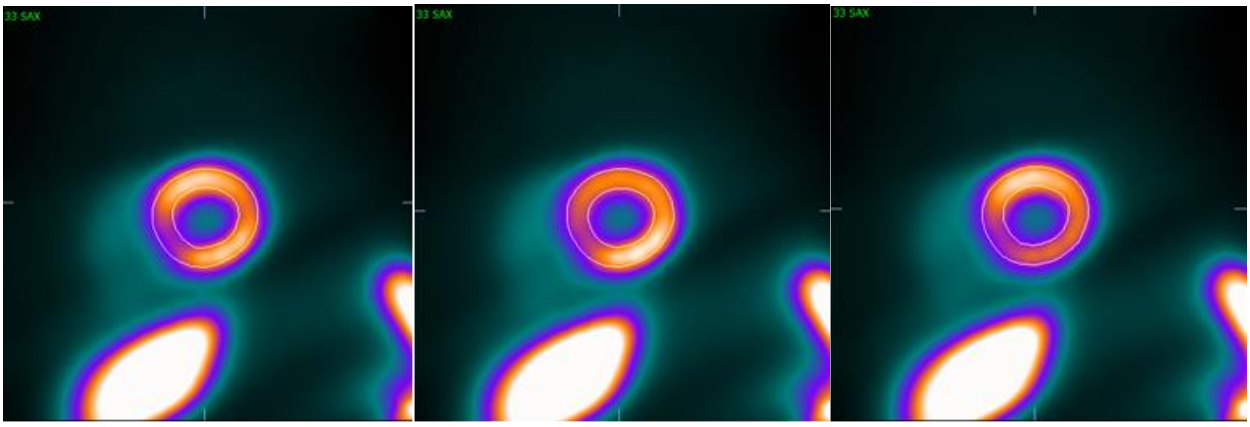

With Lesion $\Theta = 90^{\circ}$ With Lesion $\Theta = 270^{\circ}$

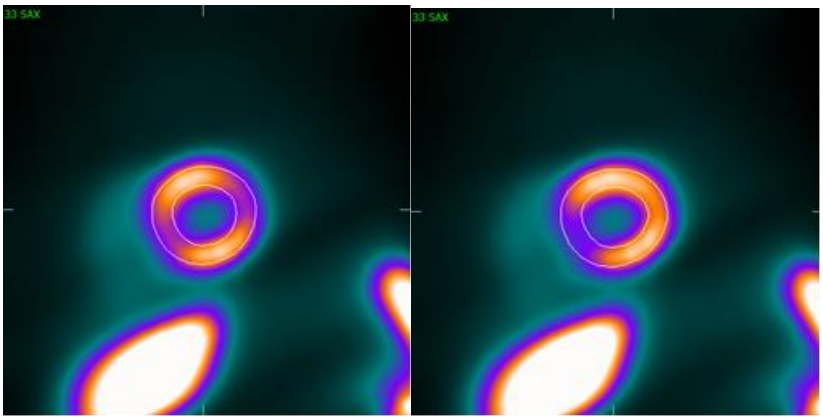

Figure 24. Short-axis images of ideal reconstruction without lesion and with lesions at four locations.

The reconstructed short-axis images of a particular cardiac and respiratory gate for AVE-AC and RMM-AC are shown in Figure 25 with the ideal recon images. The RMM-AC images seem to have limited improvement over that of AVE-AC. We further plotted the intensity profiles (along the red lines in Figure 25) in Figure 26, we present line profiles that traverse the entirety of the heart for each of the four female cases. RMM-AC profiles show a better match with the ideal recon than that of AVE-AC.

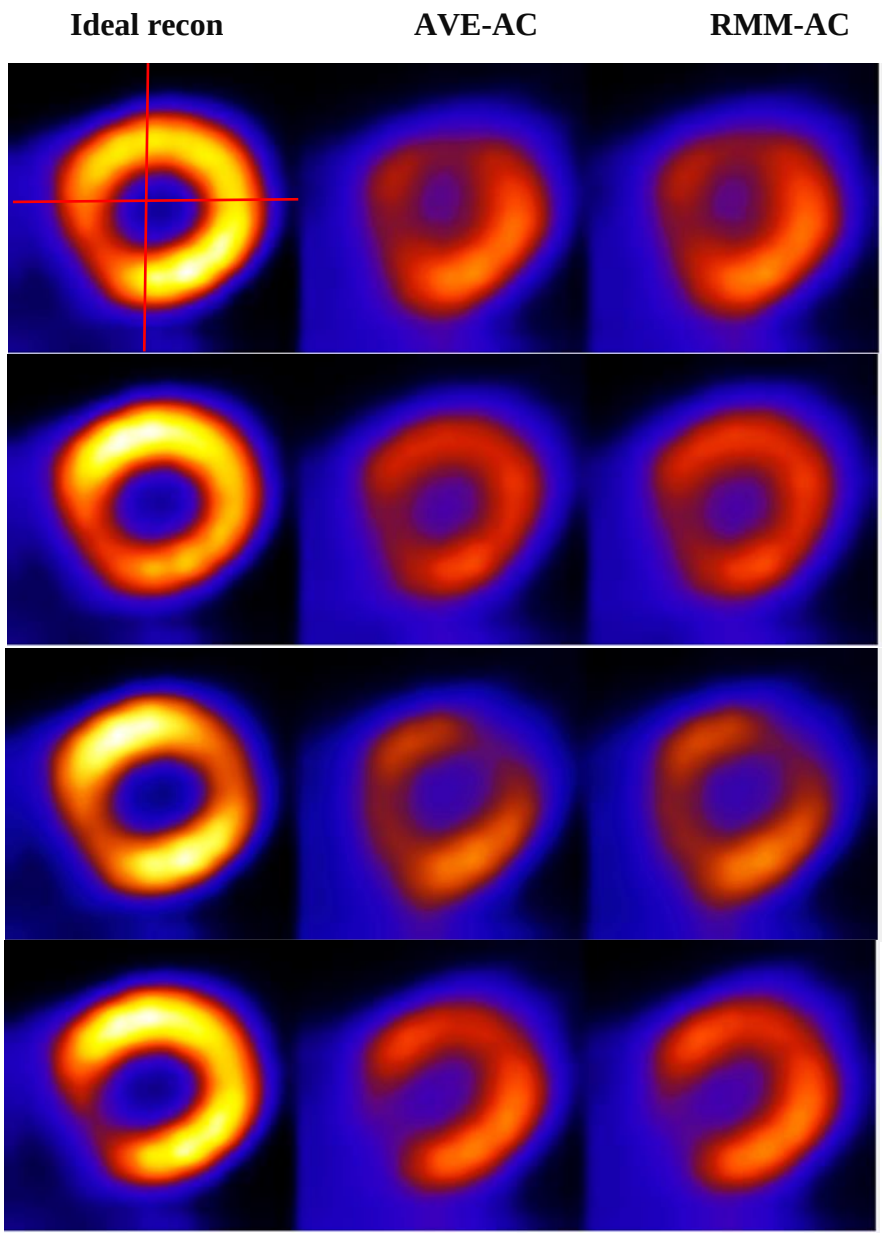

Figure 25. Reconstructed short axis images for four lesion locations at a particular cardiac and respiratory gate using different AC methods. (From top to bottom: Anterior Θ= 0°; Inferior Θ= 180°; Lateral Θ= 90°; Septal Θ= 270°)

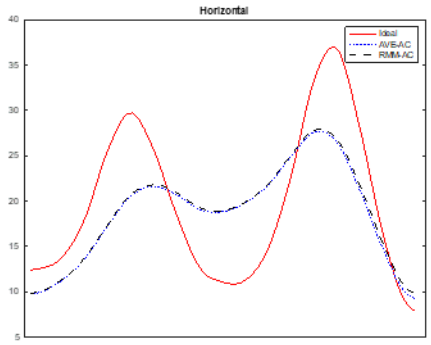

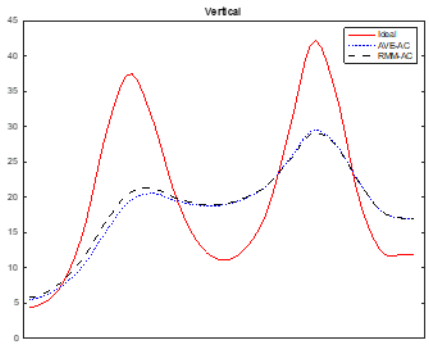

(a) Anterior lesion

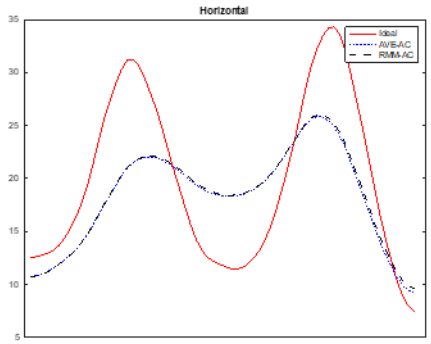

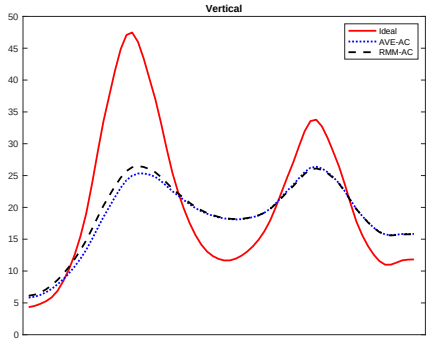

(b) Inferior Lesion

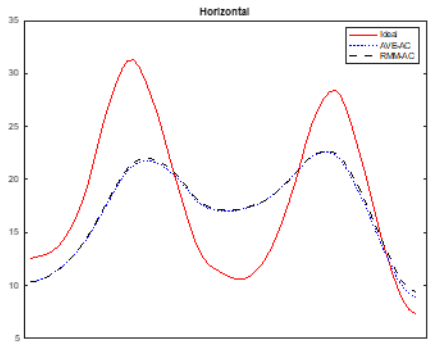

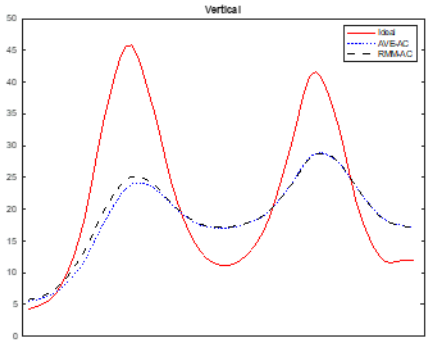

(c) Lateral lesion

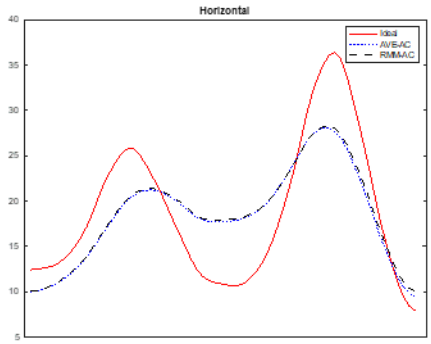

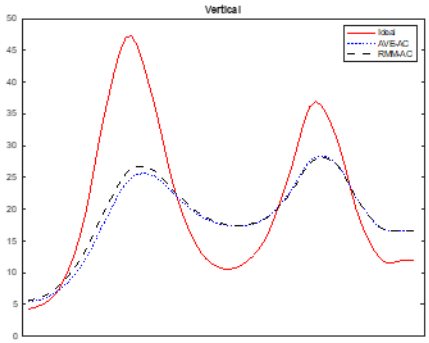

(d) Septal Lesion

Figure 26. The line profile for four different lesion cases

To quantitatively evaluate the performance of AVE-AC and RMM-AC, we calculated RMSE and Az in Table 2. As can be seen, RMM-AC outperforms AVE-AC in both metrics, which reflects improvements on both reconstruction accuracy and lesion detectability. Our findings from Table 2 demonstrate that RMM-AC for D-SPECT can further improve the quantification (RMSE) and diagnostic accuracy (Az) over AVE-AC.

Table 2. RMSE and CHO Results

Lesion Locations	**Metrics \ Method**	**Averaged AC**	**Matched AC**
Anterior	RMSE	8.1425	7.7134
$\Theta = 0°$	Az	0.7081	0.7377
Inferior	RMSE	7.2904	7.0264
$\Theta = 180°$	Az	0.789	0.791
Lateral	RMSE	7.2677	6.8345
$\Theta = 90°$	Az	0.773	0.8351
Septal	RMSE	7.3653	6.9494
$\Theta = 270°$	Az	0.7631	0.7869

CHAPTER 5 Conclusion and Future Work

Our simulation results suggest that matched attenuation correction can further improve D-SPECT which takes both cardiac and respiratory motion into reconstruction. This study is very computationally intensive. All reconstructions on the Frontera CPU server at TACC [44], where the Channelized Hotelling Observer (CHO) calculations need 30 noise realizations for each case (1 without lesion + 4 lesion locations = 5 cases), were distributed across 30 nodes. Each node was equipped with an Intel Xeon Platinum 8280 processor and 192GB of memory. The overall computation time for each recon averaged around 6 hours. This equates to a total of 1800 node hours to complete one experiment, considering two approaches (AVE-AC and RMM-AC) across five cases.

Moreover, our study adaptes reconstruction methodology as "feedback-reconstruction". This innovative approach represents a paradigm shift in SPECT image reconstruction, offering a versatile framework for addressing motion artifacts and enhancing image fidelity. The initial 3D reconstruction method, which is focused on cardiac motion reconstruction, is based on noisy motion data and can provide a coarse reconstruction image. After generating the initial set of reconstruction images, we apply a motion estimation method specifically designed for cardiac/respiratory motion. During this stage, information from other images is fused into the target image. Subsequently, the fused image undergoes another round of reconstruction, which solely concentrates on its own projection. The objective of this step is to eliminate errors in motion estimation. Following this step, we can repeat step 2 for additional rounds until satisfactory results

are achieved [53].

In summary, we proposed a 4D cardiac/respiratory motion compensation reconstruction method with respiratory motion-matched AC (RMM-AC). Our results indicate that it further improves image quality over 4D reconstruction with averaged AC (AVE-AC). This transformative approach not only heralds a significant reduction in SPECT dosage but also underscores the indispensability of matched motion AC for better quantification and diagnostic accuracy of SPECT imaging. Through our exploration and innovative methodologies, we have propelled the field of SPECT imaging forward, paving the way for enhanced diagnostic capabilities and improved patient outcomes in clinical practice.

In the future, we will apply this method to real patient data collected at the University of Massachusetts Medical Center and comprehensively evaluate its improvement on D-SPECT diagnostic accuracy.

REFERENCES

1. Wernick, Miles N., and John N. Aarsvold. Emission Tomography the Fundamentals of Pet and Spect. Elsevier Academic Press, 2004.

2. Council, Staff National Research. Mathematics and Physics of Emerging Biomedical Imaging. National Academies Press, 1996.

3. Hoberück, Sebastian, et al. "One Hundred Years of The Tracer Principle." Journal of Nuclear Medicine, Society of Nuclear Medicine, 26 Oct. 2023, jnm.snmjournals.org/content/early/2023/10/26/jnumed.123.266458.

4. Hevesy G. The absorption and translocation of lead by plants: a contribution to the application of the method of radioactive indicators in the investigation of the change of substance in plants. *Biochem J*. 1923;17:439–445.

5. Feld M, de Roo M. Geschichte der Nuklearmedizin in Europa. Schattauer; 2000:11–12.

6. Rutherford E. The scattering of α and β particles by matter and the structure of the atom. Lond Edinb Dublin Philos Mag J Sci. 1911;21:669–688

7. Livieratos, Lefteris. "Basic Principles of SPECT and Pet Imaging." SpringerLink, Springer Berlin Heidelberg, 1 Jan. 1970, link.springer.com/chapter/10.1007/978-3-642-02400-9_12.

8. Patel, Jigar J. "Myocardial Perfusion Scan." StatPearls [Internet]., U.S. National Library of Medicine, 14 Aug. 2023, www.ncbi.nlm.nih.gov/books/NBK539772/.

9. Angelidis G, Giamouzis G, Karagiannis G, Butler J, Tsougos I, Valotassiou V, Giannakoulas G, Dimakopoulos N, Xanthopoulos A, Skoularigis J, Triposkiadis F, Georgoulias P. SPECT and PET in ischemic heart failure. Heart Fail Rev. 2017 Mar;22(2):243-261

10. Iskandrian AS. Single-photon emission computed tomographic thallium imaging with adenosine, dipyridamole, and exercise. Am Heart J. 1991 Jul;122(1 Pt 1):279-84; discussion 302-6.

11. Jaarsma C, Leiner T, Bekkers SC, Crijns HJ, Wildberger JE, Nagel E, Nelemans PJ, Schalla S. Diagnostic performance of noninvasive myocardial perfusion imaging using single-photon emission computed tomography, cardiac magnetic resonance, and positron emission tomography imaging for the detection of obstructive coronary artery disease: a meta-analysis. J Am Coll Cardiol. 2012 May 08;59(19):1719-28.

12. Pelletier-Galarneau M, Martineau P, El Fakhri G. Quantification of PET Myocardial Blood Flow. Curr Cardiol Rep. 2019 Feb 28;21(3):11.

13. Slomka P, Xu Y, Berman D, Germano G. Quantitative analysis of perfusion studies: strengths and pitfalls. J Nucl Cardiol. 2012 Apr;19(2):338-46.

14. Shanoudy H, Raggi P, Beller GA, Soliman A, Ammermann EG, Kastner RJ, Watson DD. Comparison of technetium-99m tetrofosmin and thallium-201 single-photon emission computed tomographic imaging for detection of myocardial perfusion defects in patients with coronary artery disease. J Am Coll Cardiol. 1998 Feb;31(2):331-7.

15. Jin, Mingwu, et al. "4D Reconstruction for Low-Dose Cardiac Gated SPECT." Medical Physics, U.S. National Library of Medicine, Feb. 2013,

16. Henzlova, M.J., et al., ASNC imaging guidelines for SPECT nuclear cardiology procedures: Stress, protocols, and tracers. Journal of Nuclear Cardiology, 2016. 23(3): p. 606-639.

17. Shojaeifard, Maryam, et al. "Comparison of Gated SPECT Myocardial Perfusion Imaging with Echocardiography for the Measurement of Left Ventricular Volumes and Ejection Fraction in Patients with Severe Heart Failure." Research in Cardiovascular Medicine, U.S. National Library of Medicine, 19 Dec. 2015.

18. Patton, James A., and Timothy G. Turkington. "SPECT/CT Physical Principles and Attenuation Correction." Journal of Nuclear Medicine Technology, Society of Nuclear Medicine, 1 Mar. 2008, tech.snmjournals.org/content/36/1/1.

19. Beller, G.A. and B.L. Zaret, Contributions of Nuclear Cardiology to Diagnosis and Prognosis of Patients with Coronary Artery Disease. Circulation, 2000. 101(12): p. 1465-1478.

20. DePuey EG, Rozanski A. Using gated technetium-99m-sestamibi SPECT to characterize fixed myocardial defects as infarct or artifact. J Nucl Med.1995; 36:952–955.

21. Vanzetto G, Calnon DA, Ruiz M, Watson DD, Pasqualini R, Beller GA, Glover DK. Myocardial uptake and redistribution of 99mTc-N-NOET in dogs with either sustained coronary low flow or transient coronary occlusion: comparison with 201Tl and myocardial blood flow. Circulation.1997; 96:2325–2331.

22. Taillefer R, DePuey EG, Udelson JE, Beller GA, Latour Y, Reeves F. Comparative diagnostic accuracy of Tl-201 and Tc-99m sestamibi SPECT imaging (perfusion and ECG-gated SPECT) in detecting coronary artery disease in women. J Am Coll Cardiol.1997; 29:69–77.

23. Germano G, Erel J, Kiat H, Kavanagh PB, Berman DS. Quantitative LVEF and qualitative regional function from gated thallium-201 perfusion SPECT. J Nucl Med.1997; 38:749–754.

24. Calnon DA, Kastner RJ, Smith WH, Segalla D, Beller GA, Watson DD. Validation of a new counts-based gated single photon emission computed tomography method for quantifying left ventricular systolic function: comparison with equilibrium radionuclide angiography. J Nucl Cardiol.1997; 4:464–471.

25. Maddahi J, Kiat H, Friedman JD, Berman DS, Van Train KF, Garcia EV. Technetium-99m-sestamibi myocardial perfusion imaging for evaluation of coronary artery disease. In: Zaret BL, Beller GA, eds. Nuclear Cardiology: State of the Art and Future Directions. 1st ed. St Louis, Mo: Mosby-Year Book; 1993:191–200.

26. Travin, M.I., Pitfalls and Limitations of Radionuclide and Hybrid Cardiac Imaging. Seminars in Nuclear Medicine, 2015. 45(5): p. 392-410.

27. Lyra, M. and A. Ploussi, Filtering in SPECT image reconstruction. Journal of Biomedical Imaging, 2011. 2011: p. Article 10.

28. Larsson, A., et al., Gaussian prefiltering of 123I DAT SPECT images when using depth-independent resolution recovery. Physics in Medicine & Biology, 2007. 52(18): p. N393.

29. Slijpen, E.T.P. and F.J. Beekman, Comparison of post-filtering and filtering between iterations for SPECT reconstruction. IEEE Transactions on Nuclear Science, 1999. 46(6): p. 2233-2238.

30. Qi, W., et al., 4-D Reconstruction With Respiratory Correction for Gated Myocardial Perfusion SPECT. IEEE Transactions on Medical Imaging, 2017. 36(8): p. 1626-1635.

31. Hansen, C.L., et al., Myocardial perfusion and function: Single photon emission computed tomography. Journal of Nuclear Cardiology, 2007. 14(6): p. e39-e60.

32. Mariani, G., et al., A review on the clinical uses of SPECT/CT. European Journal of Nuclear Medicine and Molecular Imaging, 2010. 37(10): p. 1959-1985.

33. Kyme, A.Z. and R.R. Fulton, Motion estimation and correction in SPECT, PET and CT. Physics in Medicine & Biology, 2021. 66(18): p. 18TR02.

34. Sun J, Zhang Qi, Du Yu, et al. Dual gating myocardial perfusion SPECT denoising using a conditional generative adversarial network. Med Phys. 2022; 49: 5093–5106.

35. Underwood S, Anagnostopoulos C, Cerqueira M, et al. Myocardial perfusion scintigraphy: the evidence. Eur J Nucl Med Mol Imag. 2004; 31(2): 261-291.

36. Zhang Q, Zhang D, Mok GS. Comparison of different attenuation correction methods for dual gating myocardial perfusion SPECT/CT. IEEE Trans Radiat Plasma Med Sci. 2019; 3(5): 565-571.

37. Okuda K, Nakajima K. Has the era of dual-gated myocardial perfusion SPECT and PET arrived?. J Nucl Cardiol. 2018; 27(2): 648-650.

38. Kortelainen MJ, Koivumäki TM, Vauhkonen MJ, et al. Respiratory motion reduction with a dual gating approach in myocardial perfusion SPECT: effect on left ventricular functional parameters. J Nucl Cardiol. 2018; 25(5): 1633-1641.

39. Paul Segars, W, and Benjamin M W Tsui. "MCAT to XCAT: The Evolution of 4-D Computerized Phantoms for Imaging Research: Computer models that take account of body movements promise to provide evaluation and improvement of medical imaging devices and technology." Proceedings of the IEEE. Institute of Electrical and Electronics Engineers vol. 97,12 (2009): 1954-1968. doi:10.1109/JPROC.2009.2022417.

40. Segars, William Paul et al. "Development and application of the new dynamic Nurbs-based Cardiac-Torso (NCAT) phantom." The Journal of Nuclear Medicine 42 (2001): 174-205.

41. Ljungberg, M., S. Strand, and M. King, The SIMIND Monte Carlo program. Monte Carlo calculation in nuclear medicine: Applications in diagnostic imaging, 1998: p. 145-163.

42. Brankov, J.G., Evaluation of the channelized Hotelling observer with an internal-noise model in a train-test paradigm for cardiac SPECT defect detection. Physics in Medicine & Biology, 2013. 58(20): p. 7159.

43. Brankov, Jovan G et al. "Learning a channelized observer for image quality assessment." IEEE transactions on medical imaging vol. 28,7 (2009): 991-9. doi:10.1109/TMI.2008.2008956

44. Stanzione, D., et al., Frontera: The Evolution of Leadership Computing at the National Science Foundation, in Practice and Experience in Advanced Research Computing. 2020, Association for Computing Machinery: Portland, OR, USA. p. 106–111.

45. King MA, Miller TR. Use of nonstationary Wiener filter in nuclear medicine. Eur J Nucl Med. 1985;10:458–461.

46. Lalush DS, Tsui BMW. Block-iterative techniques for fast 4D reconstruction using a prior motion models in gated cardiac SPECT. Phys Med Biol. 1998;43:875–886.

47. Gilland D, Mair B, Bowsher J, Anderson J. Simultaneous reconstruction and motion estimation for gated cardiac ECT. Nuclear Science Symposium Conference Record, 2001 IEEE. 2001;2:1069–1071

48. Gravier E, Yang Y. Motion-compensated reconstruction of tomographic image sequences. IEEE Intr Conf on Image Processing. 2003;2:807–810.

49. Mitra D, Eiland D, Abdallah M, Bouthcko R, Gullberg GT, Schechtmann N. SinoCor: motion correction in SPECT. Society of Photo-Optical Instrumentation Engineers (SPIE) Conference Series. 2012 Feb;8314:52–55.

50. Ueda Y, Kudomi S, Koike M, Oishi Y, Iwanaga H, Ueda K. Correction of liver displacement due to irregular respiration for SPECT images obtained using a multiple short-time acquisition with breath-holding technique. Radio Phys and Tech. 2012;5(1):71–77.

51. Kovalski G, Keidar Z, Frenkel A, Sachs J, Attia S, Azhari H. Dual "motion-frozen heart combining" respiration and contraction compensation in clinical myocardial perfusion SPECT imaging. J Nucl Cardiol. 2009;16:396–404.

52. Chan C, Harris M, Le M, Biondi J, Grobshtein Y, Liu Y-H, Sinusas AJ, Liu C. End-expiration respiratory gating for a high resolution stationary cardiac SPECT system. Phys Med Biol. 2014 Oct;59:6267–6287.

53. Zhou, Shiwei et al. "General simultaneous motion estimation and image reconstruction (G-SMEIR)." Biomedical physics & engineering express vol. 7,5 10.1088/2057-1976/ac12a4. 29 Jul. 2021, doi:10.1088/2057-1976/ac12a4